

LRG1 is an adipokine that promotes insulin sensitivity and suppresses inflammation

Chan Hee Choi

The Rockefeller University

William Barr

The Rockefeller University

Annsea Park

Yale University School of Medicine

Mascha Koenen

The Rockefeller University

Zeran Lin

The Rockefeller University

Sarah Szwed

Rockefeller University

Audrey Crane

The Rockefeller University

Thomas Carroll

The Rockefeller University

Henrik Molina

The Rockefeller University

Paul Cohen (✉ pcohen@rockefeller.edu)

The Rockefeller University <https://orcid.org/0000-0002-2786-8585>

Article

Keywords: Diabetes, insulin sensitivity, obesity, inflammation

Posted Date: July 12th, 2021

DOI: <https://doi.org/10.21203/rs.3.rs-656094/v1>

License: © ⓘ This work is licensed under a Creative Commons Attribution 4.0 International License.

[Read Full License](#)

Abstract

While dysregulation of adipocyte endocrine function plays a central role in obesity and its complications, the vast majority of adipokines remain uncharacterized. We employed bio-orthogonal non-canonical amino acid tagging (BONCAT) and mass spectrometry to comprehensively characterize the secretome of murine visceral and subcutaneous white and interscapular brown adipocytes. Over 600 proteins were identified, the majority of which showed cell type-specific enrichment. We here describe a metabolic role for leucine-rich α -2 glycoprotein 1 (LRG1) as an obesity-regulated adipokine secreted by mature adipocytes. LRG1 overexpression significantly improved glucose homeostasis in diet-induced and genetically obese mice. This was associated with markedly reduced white adipose tissue macrophage accumulation and systemic inflammation. Mechanistically, we found LRG1 binds cytochrome *c* in circulation to dampen its pro-inflammatory effect. These data support a new role for LRG1 as an insulin sensitizer with therapeutic potential given its immunomodulatory function at the nexus of obesity, inflammation, and associated pathology.

Introduction

Obesity is a major threat to human health due to its association with serious comorbidities (Angelantonio et al., 2016; Poirier et al., 2006). Now considered an important endocrine organ, adipose tissue secretes a constellation of bioactive peptides, or adipokines, many of which regulate whole-body energy homeostasis and inflammation (Funcke and Scherer, 2019). Dysregulation of adipose tissue endocrine function is a key feature of obesity and a major contributor to its sequelae. However, the vast majority of adipokines remain unstudied. Addressing this knowledge gap calls for a detailed characterization of the adipose secretome to better understand how adipocytes communicate with other cells to coordinate systemic metabolism.

Mammals possess white (WAT) and brown adipose tissues (BAT), with divergent effects on whole-body metabolism. Visceral (Visc) WAT is particularly associated with obesity-related diseases, whereas subcutaneous (SubQ) WAT is comparatively benign (Fox et al., 2007). On the other hand, active BAT is associated with improved cardiometabolic health (Becher et al., 2021; Lee et al., 2014). Whereas Visc fat contains predominantly white adipocytes that efficiently store energy, SubQ depots contain a mixture of white and thermogenic beige adipocytes which, like brown adipocytes, dissipate energy as heat via uncoupled respiration (Chouchani et al., 2019). In addition to these bioenergetic properties, transplantation studies in mice have demonstrated that secretory mediators likely convey the metabolic effects of different adipose tissues (Tran et al., 2008).

Transcriptomic profiling coupled with secretion prediction algorithms is often utilized to identify putative secreted proteins, but this approach could omit non-classically secreted factors. Alternatively, direct detection of proteins in conditioned medium (CM) can be performed using mass spectrometry (MS). Such proteomic analyses are commonly performed in fetal bovine serum (FBS)-free conditions because FBS proteins interfere with detection of relatively low abundance secreted proteins in CM. Serum

starvation, however, induces a complex and unpredictable response from cultured cells, making physiological interpretation difficult (Pirkmajer & Chibalin, 2011).

To overcome these limitations, a chemoproteomic technology called BONCAT has been applied for secretome profiling (Dieterich et al., 2006; Eichelbaum, 2012). L-Azidohomoalanine (AHA) is a non-toxic, non-canonical amino acid with structural similarity to L-methionine (Met) (Fig. 1a). AHA can be recognized by cells' native translational machinery and incorporated into the nascent proteome in place of Met. The azide functional group in AHA does not exist in nature, so peptides containing AHA can be targeted for bio-orthogonal chemical conjugation strategies called click chemistry. Applying this technique to cultured adipocytes allows for selective enrichment of low abundance nascent proteins for proteomic analysis of serum-containing CM. Here, we employed BONCAT to comprehensively profile the adipose secretome and nascent serum proteome of mice, from which we identified a novel adipokine, leucine-rich α -2 glycoprotein 1 (LRG1). LRG1 is secreted by mature adipocytes and increased in obesity. We demonstrate that LRG1 improves fasting glucose and insulin tolerance and reduces adipose tissue macrophage accumulation. At the molecular level, LRG1 binds extracellular cytochrome *c* (Cyt *c*) released from dead/dying cells and dampens Cyt *c*'s pro-inflammatory effect on macrophages. These data reveal LRG1 as a crucial regulator of metabolic health as an insulin sensitizer and suppressor of systemic inflammation in obesity.

Results

Characterization of primary adipocyte secretome

To profile the secretome of different types of primary adipocytes, stromal vascular fraction (SVF) from epididymal white adipose tissue (eWAT), inguinal white adipose tissue (iWAT), and interscapular brown adipose tissue (BAT) from C57BL/6J (B6) mice was differentiated *in vitro* into primary Visc, SubQ, and Brown adipocytes, respectively (Fig. 1b). By day 6 of differentiation, all three cell types showed comparable lipid droplet accumulation and expression of mature adipocyte markers such as *Fabp4*, *Pparg2* and *Adipoq* (Extended Data Fig. 1a,b). *In vitro* primary adipocytes recapitulated characteristic gene expression patterns *in vivo*, with expression of *Prdm16* and *Ucp1* highest in Brown, intermediate in SubQ, and lowest in Visc (Extended Data Fig. 1c). Adipocytes were pulsed with Met-deficient media containing 0.1 mM AHA and 10% FBS for 24 hours, after which CM was collected. To visualize azide-labeled secreted proteins, CM was subjected to a copper-catalyzed azide-alkyne cycloaddition (CuAAC) reaction with tetramethylrhodamine (TAMRA)-alkyne. In-gel fluorescence analysis highlighted adipocyte-derived proteins in CM as bands positive for TAMRA fluorescence (Fig. 1c).

For identification and quantitative analysis of the secretome across the three adipose cell types, azide-labeled proteins were enriched from CM by conjugating with alkyne-agarose beads. On-bead digested peptides were subjected to label-free MS. We detected a total of 742 proteins, of which 138 were excluded as reverse hits or contaminants (Extended Data Fig. 1d). The intensity-based absolute quantification (iBAQ) value estimates a protein's molar abundance, and summation of iBAQ intensities (Σ iBAQ) of a

sample can estimate total moles of proteins detected (Shin et al., 2013). Σ iBAQ values closely correlated with in-gel fluorescence, both of which showed highest abundance of secreted proteins in SubQ CM (Fig. 1d).

We next examined how many of these AHA-labeled proteins are reported or predicted secreted factors. Referencing gene ontology (GO) cellular component terms for 594 genes from 604 detected proteins, a large majority of proteins (413/594, 70%) were annotated to be extracellular (Fig. 1e). We performed retrospective secretion prediction analysis on 604 proteins, evaluating the proportion of proteins predicted to be secreted by the classical ER/Golgi pathway (SignalP5.0, TMHMM2.0), subcellular localization (DeepLoc1.0), glycosylphosphatidylinositol (GPI)-anchors (PredGPI), and non-classical routes (SecretomeP2.0) (Almagro Armenteros et al., 2017, 2019; Bendtsen et al., 2004; Krogh et al., 2001; Pierleoni et al., 2008). Over two-thirds of the proteins (413/604, 68%) were predicted to be secreted via the classical pathway, while non-classical secretion constituted about 10% (62/604) (Fig. 1f). Overall, 79% of detected proteins (479/604) met at least one criterion of secretion prediction. Notably, more than 20% of identified proteins would not have been predicted to be secreted by these algorithms, highlighting the imperfect nature of *in silico* predictions and the value of directly measuring secreted protein levels.

In-gel fluorescence analysis showed differential band patterns across the three types of adipocytes, suggesting cell type-specific secretory profiles (Fig. 1c). Consistent with this observation, principal component analysis (PCA) showed that each cell type formed a distinct cluster (Extended Data Fig. 1e). Comparing all 9 AHA-pulsed samples against each other showed higher correlations within biological replicates ($R > 0.97$) than those across different cell types ($0.74 < R < 0.91$) (Extended Data Fig. 1f). For quantitative analysis, we focused on 424 proteins detected in at least 2/3 replicates (Extended Data Fig. 1d) and compared their Log₂-transformed label-free quantification (LFQ) intensities, imputing any missing values with a left-shifted Gaussian distribution. One-way ANOVA yielded 348 proteins with significantly different ($q < 0.01$) secretory profiles across cell types, and unbiased clustering was performed based on protein levels in CM (Fig. 1g). Clusters 1 and 4 contained proteins enriched in CM of Visc and Brown, respectively. Cluster 2 proteins were most abundant in CM of SubQ followed by Visc, both white adipocytes. Cluster 3 was highly secreted by SubQ and Brown adipocytes with proteins such as SLIT2 (Svensson et al., 2016), suggesting enrichment of the beige/brown secretome. Cluster 4 comprised the largest number of proteins (125/348), consistent with Brown CM containing the greatest number of unique proteins (Fig. 1h). Ranking proteins by decreasing order of abundance, we found high levels of many well-described adipocyte-derived factors such as CFD, RETN, ADIPOQ, and RBP4 (Fig. 1i). Interestingly, many cluster 2 proteins ranked highly in abundance, while cluster 4 proteins skewed towards lower abundance (Fig. 1i). Hence, while SubQ adipocytes demonstrate high secretory capacity, the brown adipocyte secretome is characterized by a diverse array of proteins, many of which are secreted at lower levels.

We next performed pathway analysis on each of the clusters (Fig. 1j). Visc CM-enriched cluster 1 was overrepresented with proteins involved in immune response and complement activation, such as C1QA and CFH (Fig. 1k). Proteins with a role in collagen fibril organization and extracellular matrix formation,

such as COL1A1 and SFRP, were enriched in cluster 2 (Fig. 1l). Cluster 3 (beige/brown enriched) showed overrepresentation of angiogenesis regulators (Fig. 1m). Finally, cluster 4 Brown CM-specific proteins were enriched for axon guidance factors such as NRP1 and NGF, consistent with the importance of innervation in thermogenesis (Fig. 1k) (Chi et al., 2018; 2021; Wang et al., 2020; Zeng et al., 2019).

Profiling of the serum proteome *in vivo*

Previous studies have shown that AHA can be administered *in vivo* to label tissue proteins (Calve et al., 2016; McClatchy et al., 2015). However, it has not been tested whether this method can label the nascent serum proteome. We administered 0.1 g/kg/day of AHA IP to chow-fed B6 mice for two days (Fig. 2a) and did not notice any major adverse effects based on body weight (Fig. 2b). CuAAC conjugation of serum proteins with TAMRA-alkyne and in-gel fluorescence analysis showed increased signal across most bands in the AHA group along with some AHA group-specific fluorescent bands (Fig. 2c). We used alkyne-agarose beads to enrich the azide-labeled nascent proteome and performed MS analysis. Σ IBAQ showed successful enrichment in animals injected with AHA (Fig. 2d). Even without dietary Met restriction or depletion of abundant serum proteins, we were able to identify and quantitate 180 proteins, including classical adipokines such as ADIPOQ, adipsin (CFD), and RBP4 (Fig. 2e).

Because AHA can be incorporated into the proteome of any tissue, we employed bioinformatic analyses to predict the source of serum proteins. We cross-referenced 177 genes from 180 detected proteins with publicly available transcriptomic datasets, such as ENCODE (RNA-Seq based) and BioGPS (microarray based) (Davis et al., 2018; Wu et al., 2016). A t-distributed stochastic neighbor embedding (t-SNE) plot was generated with each protein and its tissue mRNA levels from the ENCODE/LICR dataset (Fig. 2f). The majority of proteins were most highly expressed by the liver, which comprised the largest cluster (98/177, 55%). BAT, the only adipose tissue profiled in the dataset, formed a cluster of 14 genes (7.9%). As expected, classical adipokines known for highly adipose-specific expression such as adiponectin (*Adipoq*) and adipsin (*Cfd*) belonged to this group, along with a recently described batokine, *Kng2* (Peyrou et al., 2020).

BioGPS offers microarray-based transcriptomic data across a much wider variety of mouse tissue and cell types, including eWAT and BAT. We numerically scaled the degree of adipose tissue enrichment for each detected serum protein. Adipose enrichment of a gene was defined as the number of tissues with expression lower than that of eWAT, BAT, or combined. We divided this value by the total number of pairwise comparisons (i.e., total number of tissues - 2 adipose tissues) to obtain the percentage adipose tissue enrichment score. Among the top-enriched genes were well-described adipokines such as *Adipoq*, where 76 of 86 tissues (88.4%) expressed *Adipoq* at significantly lower levels than eWAT and BAT combined (Fig. 2g). We also identified genes yet to be described as adipokines, such as *Lrg1* and *H2-Q10* (Fig. 2g). Many genes, such as *Rbp4*, *Agt*, and *Lrg1*, showed high expression in adipose tissues as well as liver. On the t-SNE plot, these genes were grouped with other liver-specific genes, but located closer to the adipose tissue cluster (Fig. 2f). Still, their percentage enrichment scores were > 80%, as few other tissues express those genes.

LRG1 is secreted by mature adipocytes and increased in obesity

To identify uncharacterized adipokines with a putative role in whole-body metabolism, we prioritized factors 1) detected in adipocyte CM, 2) present in the nascent serum proteome, and 3) enriched in adipose tissues with scores > 80% (Fig. 3a). This analysis yielded 10 proteins (Fig. 3a). ADIPOQ, CFD, and RBP4 have already been identified as adipokines, validating our search strategy. Haptoglobin (HP), ceruloplasmin (CP), and angiotensinogen (AGT) have well-characterized biological functions. We therefore focused on LRG1, a protein with relatively unknown metabolic function.

LRG1, or leucine-rich α -2 glycoprotein 1, has been shown to be expressed in endothelial cells, where it promotes angiogenesis by modulating TGF- β signaling (Wang et al. 2013). However, LRG1 has not been characterized as an adipokine, nor has its role in whole-body metabolism been studied. Consistent with our tissue enrichment analysis, qPCR of mouse tissues showed that *Lrg1* mRNA was mostly expressed in adipose tissues and liver (Fig. 3b). To determine which cell type(s) within adipose tissue express *Lrg1*, we fractionated eWAT, iWAT, and BAT to separate floating mature adipocytes from the SVF. *Adipoq*, a mature adipocyte marker, was significantly co-enriched with *Lrg1* in the adipocyte fraction in all three depots (Fig. 3c and Extended Data Fig. 2a). Finally, we cultured primary Visc, SubQ, and Brown adipocytes and confirmed that *Lrg1* mRNA is induced > 70-fold in all three cell types during *in vitro* adipogenesis (Fig. 3d). Consistent with mRNA data, we found robust levels of LRG1 protein in CM of mature adipocytes, whereas preadipocytes did not secrete detectable LRG1 (Fig. 3e). Of note, LRG1 protein levels detected by western blot were consistent with MS results (Extended Data Fig. 2b).

To assess whether adipose tissues are a significant contributor to circulating LRG1 levels, we collected serum from chow-fed lean mice or diet-induced obese (DIO) mice on high fat diet (HFD) for 4 or 9 weeks. Serum LRG1 protein levels increased with age and obesity (Fig. 3f). qPCR of major *Lrg1*-expressing tissues showed significant induction of *Lrg1* mRNA in iWAT of DIO mice, but not in liver (Fig. 3g). With iWAT expansion in obesity, this induction likely contributes to elevated serum LRG1 levels in this state. Obesity is characterized by chronic low-grade inflammation, with elevated circulating inflammatory cytokines (Lackey and Olefsky, 2016). We observed that treatment of primary SubQ adipocytes with recombinant TNF α induced expression of *Lrg1* mRNA and protein in CM (Fig. 3h,i). Taken together, these results demonstrate that LRG1 is an obesity-induced adipokine.

LRG1 overexpression improves glucose homeostasis in diet-induced obesity

To explore whether LRG1 as an adipokine affects whole-body energy homeostasis, we used viral vectors to overexpress LRG1 *in vivo*. Adenovirus encoding eGFP (Ad-eGFP) or C-terminally FLAG-tagged LRG1 (Ad-LRG1-FL) was administered to obese B6 mice on HFD for 10 weeks (Fig. 4a). Plasma western blot confirmed LRG1 overexpression in the Ad-LRG1-FL group 5 days after infection (Fig. 4b). We observed no difference in body weights between groups (Fig. 4c), but an insulin tolerance test (ITT) showed that the Ad-LRG1-FL group had significantly enhanced insulin response ($P = 0.045$) (Fig. 4d).

To study the longitudinal effects of chronic LRG1 overexpression, we used AAV8, which has tropism for liver and adipose tissue. We administered AAV-eGFP or AAV-LRG1-FL to 6-week-old male B6 mice (Fig. 4e)

and confirmed increased plasma LRG1 in the latter (Fig. 4f). During 3 months of HFD, both groups gained an equivalent amount of weight to around 50 g (Fig. 4g), with no difference in tissue weights (Fig. 4h). Fasting glucose measurements from 4 to 14 weeks on HFD showed that the AAV-LRG1-FL group had significantly lower fasting glucose levels ($P=0.0097$) with a dampened peak (LRG1: 225.9 ± 6.5 mg/dL vs. eGFP: 263.7 ± 10.8 mg/dL, mean \pm SEM) at week 18 (Fig. 4i). A glucose tolerance test (GTT) demonstrated that AAV-LRG1-FL mice had markedly improved glucose ($P=0.0029$) (Fig. 4j) and insulin tolerance ($P=0.023$) (Fig. 4k). These observations suggest that LRG1 overexpression prevents obesity-related dysregulation of glucose homeostasis by insulin sensitization.

LRG1 loss of function elevates fasting blood glucose in diet-induced obesity

To test whether LRG1 loss of function affects glucose homeostasis, we generated whole-body LRG1-KO animals using CRISPR-Cas9 targeting exon 2 of *Lrg1* (Extended Data Fig. 3a). This led to a frameshift mutation in *Lrg1* (Extended Data Fig. 3b) and absence of LRG1 protein in plasma (Extended Data Fig. 3c). LRG1-KO (*Lrg1*^{-/-}) animals and WT (*Lrg1*^{+/+}) littermate controls on HFD showed no difference in body weight (Extended Data Fig. 3d,e) or tissue weights (Extended Data Fig. 3f). Interestingly, male LRG1-KO animals demonstrated significantly higher fasting glucose levels compared to WT littermates throughout the HFD challenge ($P=0.010$) with a higher peak (KO: 261.6 ± 11.3 mg/dL vs. eGFP: 225.0 ± 10.9 mg/dL, mean \pm SEM) at week 12 on HFD (Extended Data Fig. 3g). Therefore, fasting blood glucose levels are reciprocally regulated by LRG1 gain and loss of function. At the time points tested, however, GTT and ITT did not show significant differences between the genotypes (Extended Data Fig. 3h-k).

LRG1 overexpression delays diabetic phenotype and promotes WAT expansion in *db/db* mice

While B6 mice develop severe obesity upon HFD feeding, they demonstrate only transient and mild hyperglycemia with moderate insulin resistance (Winzell and Ahrén, 2004; Kleinert et al., 2018). Because LRG1 overexpression in B6 animals mitigated hyperglycemia, we explored whether LRG1 can improve glucose homeostasis in C57BLKS/J-*Lepr*^{db/db} (*db/db*) mice, a more extreme model of obesity-related type 2 diabetes. Due to a leptin receptor (*Lepr*) mutation and genetic background, *db/db* animals demonstrate hyperphagia and early-onset obesity, along with profound hyperglycemia and hyperinsulinemia (Kleinert et al., 2018). We confirmed that obesity and hyperglycemia over 400 mg/dL develop in *db/db* animals as early as 7 weeks of age, while littermate *misty* mice with a WT *Lepr* gene (*m/m*) maintain fasting glucose levels below 200 mg/dL (Extended Data Fig. 4a,b). Similar to B6 DIO mice, *db/db* mice showed higher circulating LRG1 levels compared to lean littermates (Extended Data Fig. 4c).

We administered AAV-eGFP or AAV-LRG1-FL to *db/db* mice at 4 weeks of age, before development of severe hyperglycemia (Fig. 5a,b). Starting two weeks post-injection, LRG1-overexpressing animals demonstrated accelerated weight gain, such that by 10 weeks of age the LRG1 group weighed 19.6% more ($P=0.004$) than eGFP controls (Fig. 5c). During this period, cages housing LRG1-overexpressing animals tended to have greater food intake (Extended Data Fig. 4d). Concomitantly, the AAV-LRG1-FL group showed delayed onset of hyperglycemia. At week 6, we observed frank hyperglycemia in eGFP animals, whereas glucose levels in the LRG1 group were 33.6% lower (eGFP: 399.5 ± 31.7 mg/dL vs.

LRG1: 265.4 ± 19.6 mg/dL, mean \pm SEM; $P = 0.0020$) (Fig. 5d). Fasting plasma insulin levels were almost halved in the LRG1 group (eGFP: 12.5 ± 1.3 ng/mL vs. LRG1: 6.3 ± 0.6 ng/mL, mean \pm SEM; $P = 0.0008$) (Fig. 5e). Consistent with these findings, an ITT showed that LRG1-overexpressing animals demonstrated significantly improved insulin sensitivity ($P = 0.019$) (Fig. 5f and Extended Data Fig. 4e). By 8 weeks of age, body weights continued to diverge between the groups, but we no longer observed significant differences in fasting blood glucose or plasma insulin concentrations (Fig. 5c-e). Tissue weight measurements revealed that LRG1-overexpressing animals had accelerated gain of eWAT ($P < 0.0001$) and iWAT ($P = 0.0001$) mass, such that by week 10, their eWAT and iWAT were 53% and 40% heavier, respectively, than those of eGFP controls (Fig. 5g,h). We observed no difference in weights of BAT, liver, or gastrocnemius muscle (Fig. 5g). These results reveal that LRG1 overexpression in *db/db* animals promotes insulin sensitivity and WAT expansion-driven weight gain.

LRG1 suppresses obesity-associated systemic inflammation

Based on the accelerated eWAT and iWAT expansion in LRG1-overexpressing *db/db* animals, we hypothesized that WAT could be a target of LRG1 action. We analyzed paraffin-embedded, hematoxylin and eosin (H&E) stained tissue sections and found that eWAT from B6 animals sacrificed at 21 weeks of age (13 weeks on HFD) was characterized by accumulation of macrophages forming crown-like structures (CLS) (Fig. 6a). The distal portion of eWAT was especially susceptible to CLS formation in eGFP controls, while the same region in LRG1-overexpressing animals displayed an 82% reduction in CLS number ($P < 0.0001$) (Fig. 6a,b). B6 iWAT contained fewer CLS compared to eWAT and did not show major morphological differences between groups (Extended Data Fig. 5a,b). In *db/db* eWAT, we observed significantly reduced CLS in the LRG1 group by 81% at week 7 ($P = 0.0001$) and 85% at week 10 ($P < 0.0001$) (Fig. 6c,d). Similarly, CLS in *db/db* iWAT from LRG1-overexpressing animals were reduced by 83% at week 7 ($P = 0.0043$) and 88% at week 10 ($P < 0.0001$) (Fig. 6c,e).

Obesity is associated with non-alcoholic fatty liver disease (NAFLD), characterized by hepatic steatosis with or without inflammation (Farrell et al., 2019). While HFD-fed B6 mice rarely demonstrate liver injury or inflammation, mild necroinflammation can be observed in *db/db* liver as early as 1 month of age (Febbraio et al., 2019; Trak-Smayra et al., 2011). Liver sections from the B6 cohort showed a similar degree of steatosis in both groups, without any inflammatory lesions (Extended Data Fig. 5c). In the *db/db* cohort, while both eGFP and LRG1 developed a similar degree of hepatosteatosis, inflammatory foci were found only in eGFP-expressing animals (Fig. 6c).

Inflammation is a key link between obesity and insulin resistance (Saltiel & Olefsky, 2017). We hypothesized that LRG1 may mediate its insulin sensitizing effect via attenuation of inflammation in susceptible organs. We performed RNA-Seq analysis on eWAT from AAV-treated *db/db* animals harvested at week 7 (midpoint) and 10 (endpoint). We performed differential gene expression analysis between the eGFP and LRG1 groups at midpoint and subjected the list of significant genes ($P < 0.01$) to GO gene-set enrichment analysis (GSEA). All of the top 20 differentially regulated pathways showed highly significant enrichment ($P = 0.0067$) and were immune-related, including leukocyte activation, innate immune response, and cytokine production (Fig. 6f). The enrichment score for each of these pathways was

negative in the LRG1 group, indicating down-regulation of inflammatory processes in these animals. GSEA of significantly regulated genes at the 10-week endpoint yielded similar down-regulation of immune-related pathways in the LRG1 group (Extended Data Fig. 5d). To visualize which genes are most significantly differentially regulated, we plotted a heatmap of 68 genes that showed significant difference (adjusted $P < 0.01$) with Log₂ fold-change of > 2 or < -2 between the two groups at both time points. Consistent with the pathway analysis, the LRG1 group showed significant down-regulation of cytokines and chemokines such as *Ccl3*, *Ccl4*, and *Cxcl9*; metalloproteinases such as *Mmp12* and *Mmp13* known to be highly expressed by macrophages; and various immunoglobulin subunit genes (Fig. 6g).

Our histological analysis demonstrated significantly reduced CLS in eWAT of LRG1-overexpressing animals. Deconvolution algorithms such as CIBERSORTx allow estimation of cell populations from bulk RNA-Seq datasets (Newman et al., 2019). We performed CIBERSORTx analysis on the expression dataset to gain further insight into differences in immune cell populations. CIBERSORTx estimated that the LRG1 group contains fewer immune cells (Fig. 6h). Macrophages were predicted to constitute the majority of immune cells in every eWAT sample analyzed, and the LRG1 group demonstrated a lower absolute quantity of macrophages (Fig. 6h), without affecting their relative proportions (Extended Data Fig. 5e). Many of the differentially regulated genes between eGFP- and LRG1-overexpressing animals encode chemokines and cytokines. We performed a multiplex cytokine assay to assess whether these differences are reflected in serum levels, and at midpoint (week 7), the LRG1 group showed 28–86% reduction of circulating chemokines such as MCP-1, MIP-1 α , MIG, and IP-10 and cytokines such as TNF α and IFN γ (Fig. 6i). Many of these differences subsided by week 10, mostly due to a reduction of cytokines in the eGFP group (Extended Data Fig. 5f). Taken together, these results suggest that LRG1-overexpression attenuated pro-inflammatory processes associated with obesity.

LRG1 binds extracellular cytochrome *c* and blocks its pro-inflammatory effect on macrophages

LRG1 contains leucine-rich repeat (LRR) domains, which form a structural framework for protein-protein interactions. We hypothesized that LRG1's immunomodulatory function is mediated by protein-protein interactions. LRG1 has been reported to bind cytochrome *c* (Cyt *c*), a mitochondrial protein (Cummings et al., 2006), but the physiological significance of this interaction has not been studied. In addition to its role in the respiratory chain and intrinsic apoptosis pathway, Cyt *c* is released into the extracellular space following cell death (Jemmerson et al., 2002; Renz et al., 2001) and mediates pro-inflammatory signals as a damage-associated molecular pattern (DAMP) (Grazioli & Pugin, 2018). Adipocyte death in obesity is a key event promoting macrophage infiltration and WAT inflammation (Cinti et al., 2005), but the exact triggers of metabolic inflammation remain unidentified. We explored whether extracellular Cyt *c* released by dead/dying adipocytes could be a key mediator of macrophage recruitment/activation, and if LRG1 in turn modulates the pro-inflammatory action of Cyt *c*.

We first examined whether LRG1 binds extracellular Cyt *c* in the circulation. We utilized the C-terminal FLAG-tag of overexpressed LRG1 and α -FLAG antibody-conjugated beads to co-immunoprecipitate (IP) LRG1-FL and interacting partners. In the serum of *db/db* animals transduced with AAV-LRG1-FL, we were

able to successfully co-IP both LRG1-FL and Cyt *c* from the serum, indicating the two proteins indeed circulate as a complex (Fig. 7a). While elevated Cyt *c* levels in circulation have been observed in conditions involving cell death or inflammation (Adachi et al., 2004; Alleyne et al., 2001; Barczyk et al., 2005; Ben-Ari et al., 2003), it is not known whether obesity is associated with increased serum Cyt *c* levels. Western blot analysis of serum revealed that Cyt *c* is increased in *db/db* animals compared to lean littermates (Fig. 7b). Interestingly, extracellular Cyt *c* levels trended higher at 7 than at 10 weeks of age (Fig. 7b), correlating with the time point when LRG1 overexpression has a potent physiological effect. In B6 mice, HFD led to increased Cyt *c* levels compared to chow-fed lean animals (Fig. 7c). To test if dying adipocytes can contribute to circulating Cyt *c*, we subjected primary SubQ adipocytes to treatments that induce apoptosis or necrosis (Fig. 7d). In CM of SubQ adipocytes treated with staurosporine (STS) for 24 h, we detected a robust increase in Cyt *c* compared to vehicle controls (Fig. 7d). CM collected from adipocytes incubated in hypoxic conditions or treated with TNF α also showed increased Cyt *c* compared to normoxic or vehicle controls, respectively (Fig. 7d).

Extracellular Cyt *c* has been shown to exert a pro-inflammatory effect by acting on the toll-like receptor 4 (TLR4)-mediated innate immune signaling pathway in astrocytes (Wenzel et al., 2019). Because circulating monocytes contribute to adipose tissue macrophages in obesity (Oh et al., 2012), we tested whether bone-marrow derived macrophages (BMDMs) respond to extracellular Cyt *c* by upregulating pro-inflammatory genes. Treating BMDMs with horse Cyt *c* led to > 30-fold induction of lipopolysaccharide (LPS)-responsive pro-inflammatory genes such as *Il1b*, *Cxcl10*, *Il6*, and *Nos2* ($P < 0.0001$), while pre-treatment of macrophages with a small molecule TLR4 inhibitor, TAK-242, prevented this induction (Fig. 7e). These data confirm that Cyt *c* in the extracellular space acts as a DAMP that activates innate immune signaling and polarizes macrophages into a more pro-inflammatory state. We then explored how co-treatment of Cyt *c* and recombinant human LRG1 (rhLRG1) affects Cyt *c*'s pro-inflammatory effect on macrophages. Prior to treatment, media containing Cyt *c*, rhLRG1, or both were incubated for one hour to allow protein-protein interactions to occur. Compared to single treatment, co-treatment with rhLRG1 significantly dampened Cyt *c*-mediated induction of *Il1b* ($P < 0.0001$), *Cxcl10* ($P = 0.024$), and *Il6* ($P = 0.0008$), while *Nos2* induction was not affected by co-treatment with rhLRG1. (Fig. 7f). Interestingly, pre-treatment of BMDMs with rhLRG1 followed by addition of Cyt *c* did not attenuate the latter's pro-inflammatory effect, suggesting that Cyt *c*-LRG1 complex formation is necessary for LRG1's modulatory effect (Extended Data Fig. 6a). Hence, LRG1 can modulate the pro-inflammatory gene expression responses induced by Cyt *c*.

Cyt *c* is a small (12.5 kDa), globular protein with a short half-life in circulation (Radhakrishnan et al., 2007). Small proteins such as Cyt *c* are expected to be rapidly cleared via glomerular filtration in the kidney. With the tight binding interaction between LRG1 and Cyt *c*, we hypothesized that much of extracellular Cyt *c* circulates as a complex with LRG1. To assess whether this interaction affects Cyt *c* clearance, we performed retroorbital injection of horse Cyt *c* into WT and LRG1-KO mice and collected blood at time points from 5 minutes to 6 hours post-injection. Plasma western blot showed that LRG1-KO animals almost completely cleared Cyt *c* by 2 hours, whereas in WT animals, an initial decrease in Cyt *c* was followed by nearly constant levels between 1 and 4 hours post-injection (Fig. 7g). Fitting one-phase

decay functions to relative Cyt *c* intensities showed that while both WT and LRG1-KO curves have similar half-lives (WT: 16.10 min vs. KO: 17.32 min), the WT trace plateaus at 0.2791, whereas the LRG1-KO curve approaches zero (Fig. 7h and Extended Data Fig. 6b). Concomitantly, appearance of Cyt *c* in the urine was observed as soon as 30 minutes after the injection, demonstrating that clearance of excess Cyt *c* is indeed through the kidneys (Extended Data Fig. 6c). Urine Ponceau S staining showed that detected proteins were all below 25 kDa, the apparent size limit for urinary excretion (Extended Data Fig. 6c). We reason that in LRG1-KO animals, Cyt *c* circulates as an unbound, free form that can be rapidly excreted by glomerular filtration, whereas the presence of LRG1 in WT animals prevents a portion of Cyt *c* from excretion due to formation of a complex larger than the size cutoff for glomerular filtration. Taken together, these data directly demonstrate that Cyt *c* is a native ligand of LRG1, and that this interaction suppresses the pro-inflammatory effect of extracellular Cyt *c* (Fig. 7i).

Discussion

We applied a chemoproteomic technology to comprehensively profile the secretome of three major types of murine primary adipocytes, revealing unique secretory profiles of each cell type with differential functional enrichment. This method was also applied *in vivo* to profile the nascent serum proteome, and bioinformatic analysis demonstrated that adipose tissue is an important contributor to the serum proteome. The intersection of the adipocyte and serum proteome included classical adipokines such as adiponectin (Wang and Scherer, 2016), adipsin (Lo et al., 2014; Gómez-Banoy et al., 2019), and RBP4 (Yang et al., 2005), all of which have important roles in whole-body energy homeostasis. LRG1 shares a similar expression signature with these adipokines, but its metabolic function has not been characterized. We demonstrate, using two types of viral vectors and two different mouse models of obesity, a novel metabolic role for LRG1 as a regulator of glucose homeostasis by promoting insulin sensitization. This insulin-sensitizing effect in LRG1 gain of function is associated with a dramatic reduction in systemic inflammation and with LRG1's ability to bind Cyt *c* and modulate its pro-inflammatory effect as a DAMP.

The low rate of intracellular proteins detected in our dataset demonstrates the advantage BONCAT provides by enabling FBS supplementation. Of the remaining 20% of proteins not predicted or annotated to be secreted, many are non-classically secreted proteins such as FABP4/5 (Hotamisligil and Bernlohr, 2015) and other novel factors we have independently confirmed as *bona fide* secreted factors. With careful validation, our dataset can greatly expand the scope of the adipose secretome that includes non-classical modes of secretion. We have also demonstrated that BONCAT can label nascent serum proteins *in vivo*. This technique can be further utilized to study the nascent serum proteome in response to stimuli difficult to model *in vitro*, such as obesity and changes in ambient temperature. Novel technologies for *in vivo* profiling of cell type-specific proteomes using non-canonical amino acids (Alvarez-Castelao et al., 2017) or proximity labeling (Branon et al., 2018; Wei et al., 2021) are on the horizon. This study provides a baseline profile of the nascent serum proteome from which cell type enrichment analyses can be performed, and bioinformatic pipelines implemented to predict tissue origin would be useful in cross-referencing with transcriptomic datasets.

Adipose tissue expansion in mice is characterized by periods of rapid adipocyte turnover, during which there is a sharp increase in adipocyte death and monocyte/macrophage accumulation (Rosen and Spiegelman, 2014; Weisberg et al., 2003). In B6 eWAT, adipocyte death and CLS formation peak around 12–16 weeks on HFD (Strissel et al., 2007), which corresponds to when a parallel surge in fasting blood glucose levels is observed. In *db/db* mice, the remodeling seems to be initiated earlier, as CLS in WAT emerge at 7 weeks of age, and chemokine/cytokine expression and circulating levels are more highly induced at week 7 than week 10. Periods when LRG1's insulin-sensitizing and anti-inflammatory effects are particularly effective coincide with these times of rapid adipocyte death and turnover. As inflammation is a key mechanistic link between obesity and insulin resistance (Saltiel & Olefsky, 2017), these findings strongly suggest LRG1 promotes insulin sensitization via modulation of inflammation during adipose tissue remodeling.

The biological context and function of LRG1 and extracellular Cyt *c* binding have been unknown. We propose LRG1 functions as a buffer against deleterious effects of extracellular Cyt *c* released from dying/dead cells. During obesity-driven adipose tissue remodeling, a rapid increase in adipocyte death contributes to increased circulating Cyt *c*, which could be an important pro-inflammatory signal triggering monocyte/macrophage recruitment. The pro-inflammatory setting of obesity also induces LRG1 in other adipocytes, and this increase in circulating LRG1 modulates inflammation by directly binding Cyt *c*. Of note, both TLR4 and LRG1 contain LRR domains, so the Cyt *c*-neutralizing effect by LRG1 could involve steric interference as the two proteins compete for binding Cyt *c*. While the current study focused on LRG1's effect on adipose tissue, it is important to emphasize that LRG1-mediated anti-inflammatory effects were systemic, as observed by the decrease in inflammatory foci in LRG1-overexpressing *db/db* liver. As hepatocyte apoptosis contributes to progression of NASH (non-alcoholic steatohepatitis) in NAFLD (Feldstein et al., 2003), further investigation may uncover a hepatoprotective role for LRG1 in NAFLD. Multiple biomarker studies in humans have shown that increased LRG1 is associated with not only obesity (Pek et al., 2018) but also conditions involving cell death and inflammation, such as appendicitis (Kentsis et al., 2010), solid tumors (Belczacka et al., 2019) and autoimmune diseases (Naka and Fujimoto 2018). Our study suggests that induction of LRG1 in these settings could be a compensatory mechanism to modulate inflammation.

Enhanced renal clearance of Cyt *c* in LRG1-KO mice provides further evidence that LRG1 complexes with Cyt *c* in circulation and highlights the need to measure LRG1 levels in future studies utilizing extracellular Cyt *c* as a biomarker. Similar serum Cyt *c* half-lives between WT and LRG1-KO suggest LRG1 loss of function does not affect kidney function. Divergence in Cyt *c* clearance profiles occurs towards the plateau, and we believe this difference represents the portion of Cyt *c* that stays bound to LRG1 in WT animals. Inflammation in obesity, especially in B6 DIO mice, is chronic and relatively low grade, so enhanced clearance of Cyt *c* in LRG1-KO mice could serve to counteract Cyt *c* release and protect from its deleterious effects. It is possible therefore that the effect of LRG1 loss of function may be more pronounced in conditions involving acute or high-grade inflammation.

In summary, we identified LRG1 as a novel adipokine and discovered its metabolic role as an insulin sensitizer and suppressor of inflammation. LRG1's *in vivo* function is associated with Cyt *c* binding, and this interaction sheds light on previously unappreciated molecular players of adipocyte-macrophage interaction during adipose tissue expansion and remodeling. LRG1 or targeting extracellular Cyt *c* could be an attractive therapeutic approach for treatment of not only obesity but a variety of inflammatory conditions.

Methods

Animals

C57BL/6J mice were purchased from Jackson Laboratories. C57BLKS-*Lep^{db}* homozygote males and C57BLKS-*Dock7^m* homozygote males were purchased from Jackson Laboratories. LRG1-KO (*Lrg1^{-/-}*) line was generated in C57BL/6J background by the CRISPR and Gene Editing Center at the Rockefeller University and backcrossed with C57BL/6J mice for at least five generations to minimize off-target effects. Cohorts of LRG1-KO and WT littermates for characterization studies were obtained by intercrossing male and female heterozygotes. Animals were maintained at the Rockefeller University Comparative Biosciences Center, housed at 23°C and maintained at 12 h light:dark cycles. The animals were group-housed with *ad libitum* access to food and water except during metabolic characterization studies. C57BL/6J mice were fed standard chow diet (LabDiet 5053), and where specified, started on 60% high fat diet (HFD, Research Diets D12492) feeding at 6 or 8 weeks of age. C57BLKS-*Lep^{db}* and C57BLKS-*Dock7^m* were fed standard chow diet. Virus injections were performed in designated ABSL-2 housing rooms and the transduced mice were quarantined for 72 hours post-injection before transferred to regular housing rooms. Experiments involving adenoviral and AAV8 vectors were performed in accordance with the institutional ABSL-2 guidelines. All animal studies were performed in accordance with the institutional guidelines of the Rockefeller University Institutional Animal Care and Use Committee (IACUC).

Metabolic characterization of mice

For studies involving diet-induced obesity, mouse body weights were monitored once a week, providing fresh 60% high fat diet (Research Diets) at least once a week. For fasting blood glucose measurements, mice were single housed in the morning in cages with fresh bedding and access to water but without food. Mice were kept in a procedure room free of noise or vibration throughout the experiment. After 6 h, blood was collected from the tail vein, and glucose levels were measured using a glucose meter. For plasma insulin ELISA, blood was also collected in EDTA-coated capillary tubes, which were centrifuged at 2000×g for 15 min at 4°C to collect plasma. Insulin ELISA was performed using Ultra Sensitive Mouse Insulin ELISA Kit (Crystal Chem). Glucose (GTT) and insulin tolerance tests (ITT) were performed following a similar 6 h fasting procedure and started by intraperitoneally injecting at time 0 indicated doses of glucose or Novolin R human insulin (Novo Nordisk). Following injection, blood glucose measurements were taken from the tail vein at indicated timepoints. During an ITT procedure, mice with

glucose measurements below 20 mg/dL or showing signs of hypoglycemia were rescued by 1 g/kg glucose IP injection and excluded from the study.

Generation of LRG1-KO mice

CRISPR guide RNAs were designed using CRISPOR.org (Concordet and Haeussler, 2018) and were used as two-part synthetic crRNA and tracrRNA (Alt-RTM CRISPR guide RNA, Integrated DNA Technologies, Inc). Cas9 protein, crRNA, and tracrRNA were assembled to ctRNP using protocols described previously (Shola et al., 2021). Two crRNAs were assembled to ctRNPs and electroporated to one-cell-stage mouse embryos to assess their efficiency in generating indels on the Exon 2 of *Lrg1* gene. To prepare for the microinjection mix, crRNA-B which binds to genomic target sequence “AATCTCGGTGGGACCATGGCAGG” was selected for its high on-target efficiency and low off-target potential. The final injection mix was made of 0.6 μ M of guide RNA (crRNA + tracrRNA) and 0.3 μ M of Cas9 protein according to protocols described previously (Shola et al., 2021). The injection mix was then delivered to 0.5 days of fertilized C57BL/6J mouse embryos using well-established pronuclear injection and surgical protocols (Shola et al., 2021).

Cells

Mouse primary stromal vascular fraction (SVF) cells were obtained from adipose tissues of 6- to 8-week-old male mice by collagenase digestion and plated on collagen I-coated dishes. SVF cells from epididymal white adipose tissue (eWAT) were grown in ITS media containing 1.5:1 mixture of low-glucose DMEM:MCDB201 supplemented with 2% FBS (Gemini), 1% ITS premix (Corning), 0.1 mM L-ascorbic acid 2-phosphate (Sigma), 10 ng/mL bFGF (Thermo), 0.5% penicillin/streptomycin (P/S, Gibco), and 0.2% primocin (InvivoGen). SVF cells from inguinal white adipose tissue (iWAT) and interscapular brown adipose tissue (BAT) were grown in DMEM/F-12 GlutaMAX medium (Gibco) containing 10% FBS and 1% P/S. Once grown to confluence, differentiation and maintenance of primary adipocytes across cell types were done using DMEM/F-12 GlutaMAX medium containing 10% FBS and 1% P/S. eWAT and iWAT SVF cells were induced to differentiate with an adipogenic cocktail (0.5 mM IBMX, 1 μ M dexamethasone, 1 μ M rosiglitazone, and 850 nM insulin) for the first 2 days, followed by 2 days of 1 μ M rosiglitazone and 850 nM insulin, after which the cells were maintained in 850 nM insulin for additional 2-4 days. SVF cells from BAT were differentiated as above but with 17 nM insulin. Experiments with primary adipocytes were performed between days 6 and 8 of differentiation. All cultured primary adipocytes were checked for lipid accumulation under a phase-contrast microscope before studies. Primary SVF and adipocytes were maintained at 37°C with 10% CO₂.

Bone marrow-derived macrophages (BMDMs) were obtained from 8- to 10-week-old males. Femurs and tibias were dissected, cleaned, and sterilized with ethanol before flushed of bone marrow cells, which were plated onto petri dishes. Bone marrow cells were differentiated in RPMI-1640 medium (Gibco) supplemented with 20% heat-inactivated FBS (Sigma), 1% P/S, and 100 ng/mL M-CSF (Biolegend) for 6-7 days, changing media every 2-3 days. Differentiated BMDMs were washed, trypsinized, and plated onto

TC-treated culture plates for overnight before studies were performed. Experiments with BMDMs were performed between days 6 and 7 of differentiation. BMDMs were differentiated and maintained at 37°C with 5% CO₂.

HEK293A cells were purchased from Invitrogen and grown using 4.5 g/L glucose DMEM (Gibco) supplemented with 10% FBS and 1% P/S at 37°C with 5% CO₂. Cells with passage number under 20 were used for adenovirus production. Cells were validated to be mycoplasma free.

Proteomic analysis using BONCAT

Conditioned medium generation

On day 6 of differentiation, primary adipocytes on collagen-coated 6-well plates were washed twice with warm PBS and pulsed with 1 mL/well of Met-free DMEM containing 10% dialyzed FBS, 1% P/S, 17 nM or 850 nM insulin, and either 0.1 mM AHA or 0.1 mM Met. Following 24 h incubation at 37°C with 10% CO₂, conditioned media (CM) from 6 wells (1 plate) were collected and pooled, filtered through a 0.22 µm PES membrane syringe filter unit, and supplemented with ½ tabs of EDTA-free cOmplete mini protease inhibitor cocktail (Roche) and PhosSTOP (Roche). CM was concentrated using a 3 kDa centrifugal filter unit (Millipore).

AHA administration and serum collection

Mice were injected with 0.1 g/kg/day AHA or PBS IP for 2 consecutive days and sacrificed 24 hours following the second injection. Following decapitation, truncal blood was collected, allowed to clot for 15 min at room temperature, and centrifuged at 2000×g for 15 min at 4 °C to collect serum.

In-gel fluorescence analysis

Concentrated CM or serum was dialyzed with phosphate-buffered RIPA (10 mM phosphate buffer pH 7.2, 1% Triton X-100, 0.1% Na deoxycholate, 0.1% SDS, 140 mM NaCl) supplemented with EDTA-free cOmplete mini protease inhibitor cocktail (Roche) and PhosSTOP (Roche) using a 3 kDa centrifugal filter unit (Millipore) and protein concentration was determined using Pierce BCA Protein Assay Kit (Thermo Scientific) using a dilution series of bovine serum albumin as protein standards. Copper(I)-catalyzed azide-alkyne cycloaddition reaction with TAMRA-alkyne (Invitrogen) was performed by mixing 200 µg of CM proteins with 0.1 mM TAMRA-alkyne, 1 mM TCEP, 0.1 mM TBTA, and 1 mM of CuSO₄ in phosphate-buffered RIPA and rotated end-over-end for 1 h at room temperature under protection from light. Following methanol/chloroform precipitation, the dried protein pellet was dissolved in Laemmli loading buffer. Following polyacrylamide gel electrophoresis, the gel was briefly washed with distilled H₂O and imaged with a Typhoon 5400 imager (GE Healthcare) using 532 nm excitation and a 580 nm detection filter.

Enrichment of labeled proteins

Azide-labeled nascent protein in the concentrated CM was enriched using Click-iT™ Protein Enrichment Kit (Invitrogen). Serum was diluted 1:1 with the lysis buffer provided with the kit and subjected to enrichment. Enrichment and resin wash was performed following the protocol from Eichelbaum and Krijgsveld (2014).

On-bead digestion

Extensively washed beads were incubated with Lys-C endopeptidase (Wako) in 4 M urea and 0.14 M NH_4HCO_3 by shaking at 1400 rpm for 6 h at room temperature. The resin mixture was further digested by adding trypsin (Promega) in 2 M urea and 0.14 M NH_4HCO_3 and incubated by shaking at 1400 rpm overnight at room temperature. The following day, the digestion reaction was quenched by adding trifluoroacetic acid.

LC-MS/MS

Tryptic peptides were desalted (Rappsilber et al., 2007) and separated by reverse phase nano-LC-MS/MS (column: 12cm/75um C18 built-in-emitter column, Nikkyo Technos Co., Ltd. Japan, EasyLC 1200, Thermo Scientific) using a 70-minute analytical gradient, increasing from 2% B/98% A to 38%B/62%A (A: 0.1% formic acid, B: 80% Acetonitrile/0.1% formic acid) at 300 nL/min. The mass spectrometer (Fusion Lumos, Thermo Scientific) was operated in high/high mode (120,000 and 30,000 for MS1 and MS2, respectively). Auto Gain Control was set at 50,000 for MS2. MS1 scan range was set to m/z 375-1500 and m/z 110 was set as lowest recorded mass in MS2. One-point lock mass calibration was used. All data were quantified and searched against a Uniprot mouse database using MaxQuant (v. v. 1.6.0.13) (Cox et al., 2014). Oxidation of methionine and protein N-terminal acetylation were allowed as variable modifications, cysteine carbamidomethyl was set as a fixed modification, and two missed cleavages were allowed. The “match between runs” option was enabled, and false discovery rates for proteins and peptides were set to 1%. Protein abundances measured using label free quantitation (Tyanova et al., 2016).

Proteomic data analysis

Proteomic datasets were analyzed using Perseus v1.6.14.0 (Tyanova et al., 2016). Of the detected proteins, those flagged as reverse, only identified by site, and potential contaminants were excluded from the analysis. For quantitative analysis, LFQ or iBAQ intensities were employed as indicated; LFQ intensities were used for comparisons across samples, while iBAQ intensities were used to compare abundances across different proteins. Imputation of undetected data points for $\text{Log}_2(\text{LFQ})$ intensities was performed by assigning values from a normal distribution of 0.3 width and 1.8 down shift. Principal component analysis (PCA) was performed with imputed $\text{Log}_2(\text{LFQ})$ intensities. Scatterplot representation of $\text{Log}_2(\text{LFQ})$ intensities was generated without imputation. Differentially secreted proteins were identified with ANOVA using permutation-based FDR, with FDR set at 0.01 and number of randomizations at 250.

GO cell component analysis

Gene symbols from detected proteins were submitted to Retrieve/ID mapping tool on the UniProt website (<https://uniprot.org>). List of genes that are annotated with the following gene ontology cell component terms were obtained: extracellular region (5576), extracellular space (5615), extracellular matrix (31012), plasma membrane (5886), cytosol (5829), nucleus (5634), mitochondrion (5739), endoplasmic reticulum (5783), and Golgi apparatus (5794).

Secretion prediction analysis

UniProt accession IDs of the detected proteins were submitted to Retrieve/ID mapping tool on the UniProt website (<https://uniprot.org>) to obtain the FASTA sequences, which were used as inputs for various secretion prediction algorithms using the web-based query system. We defined classically secreted proteins as having SignalP5.0 score > 0.5 and 0 or 1 predicted transmembrane domains by TMHMM2.0. Subcellular localization prediction analysis was performed using DeepLoc1.0 and searched for proteins whose predicted location is extracellular. PredGPI specificity score > 99% was used as the threshold to determine if a protein is expected to be GPI-anchored. Finally, proteins with SecretomeP2.0 score > 0.6 and SignalP5.0 score \leq 0.5 were considered non-classically secreted.

Cluster analysis and functional annotation

Hierarchical clustering was performed on z-score-transformed $\text{Log}_2(\text{LFQ})$ values using the complete-linkage method and split into 4 clusters by dendrogram. DAVID v6.8 was used to generate functional annotation of clusters (Huang et al., 2009). List of genes encoding the proteins of each of the 4 clusters were compared to a background gene list of total detected proteins in the proteomic dataset. Per cluster, top 4 overrepresented pathways in the gene ontology biological process terms were reported.

Adipose tissue enrichment analysis

To identify candidate genes enriched within brown and white adipose relative other tissue types as well to each other we used the BioGPS datasets (Su et al., 2004). The Mouse GNF1M Gene Atlas datasets (GSE1133) were downloaded from BioGPS portal (Su et al., 2004) and imported into Limma Bioconductor package (Ritchie et al., 2015) for Log_2 transformation and differential expression analysis. All pair-wise comparisons for both brown adipose and white adipose tissues against all other tissue types were performed using limma as well as the direct comparison between brown and white adipose tissues. Genes with a Log_2 fold change greater than 4 and a Benjamini-Hochberg-corrected FDR of 0.05 within pair-wise comparisons were considered significantly enriched. Genes were further scored by the total number of pair-wise comparisons where genes were found to be enriched in both adipose tissues, brown adipose tissue or white adipose tissue compared to other tissues in the tissue atlas.

RNA isolation, cDNA synthesis, and RT-qPCR

Total RNA was extracted from cultured cells using RLT buffer (Qiagen) and from tissues using TRIzol (Invitrogen) and purified using RNeasy Mini Kit (Qiagen). cDNA was synthesized from 1 µg of RNA using the High-Capacity cDNA Reverse Transcription Kit (Applied Biosciences). Power SYBR Green (Life Technologies) was used for RT-qPCR reactions performed with QuantStudio 6 Flex Real-Time PCR System (Thermo Scientific) in a 384 well format. Relative fold changes of mRNA levels were calculated using the $\Delta\Delta CT$ method with 18S rRNA as loading control. qPCR primers are provided in Supplementary Table 1.

Adipose tissue fractionation

Adipose tissues from 8-week-old C57BL/6J WT male mice were dissected and minced. eWAT and iWAT were digested in a buffer containing 10 mg/mL collagenase D (Roche), 2.4 mg/mL Dispase II (Roche), and 10 mM CaCl₂ in PBS. For BAT, 2x BAT digestion buffer containing 125 mM NaCl, 5 mM KCl, 1.3 mM CaCl₂, 5 mM glucose, 1% P/S, and 4% BSA was prepared, which was diluted 1:1 with PBS and used to dissolve collagenase B (Roche) at a final concentration of 1.5 mg/mL. Following collagenase digestion of the tissues in a 37°C water bath, the mature adipocyte fraction was separated from the SVF pellet by centrifugation at 500×g for 10 min at 4°C. The two fractions were transferred to two separate tubes, washed with DMEM/F-12 GlutaMAX containing 10% FBS and 1%P/S, and vortexed in TRIzol for RNA extraction.

RNA-Sequencing and immune cell deconvolution

Extracted RNA samples were analyzed for RNA integrity number (RIN) using the Bioanalyzer (Agilent) and sequenced using Illumina NovaSeq at the Rockefeller University Genomics Resource Center. Reads were trimmed with Cutadapt, aligned to mm10 reference genome using STAR, and quantified using featureCounts. Differential gene expression analysis was performed using DESeq2 (Love et al., 2014). Pathway analysis was performed using clusterProfiler (Yu et al., 2012). Deconvolution analysis was performed with CIBERSORTx (Newman et al., 2019) using ImmuCC signature matrix (Chen et al. 2017).

Tissue origin prediction

Mouse tissue mRNA sequencing data from ENCODE was downloaded from GSE36026. Reads were mapped and quantified as above and gene expression was normalized using DESeq2. Genes detected in mouse nascent serum were selected for t-SNE analysis. Briefly, average normalized expression in a tissue was divided by summed expression across tissues. Tissue with the highest relative expression was designated as the highest expressing tissue for a gene. t-SNE analysis was performed on relative expression values with R package Rtsne (<https://github.com/jkrijthe/Rtsne>) using a perplexity of 30 and maximum iteration of 1,000.

Immunoblot

Upon collection, conditioned medium (CM) was filtered using a 0.22 μm PES membrane syringe filter unit to remove cell debris. CM was concentrated using a 3 kDa centrifugal filter units (Millipore), and protein concentration was determined using Pierce BCA Protein Assay Kit (Thermo Scientific) using a dilution series of bovine serum albumin as protein standards. Mouse serum samples were loaded at equal volume. Pre-cast polyacrylamide gels were used for electrophoresis, after which protein was transferred to PVDF membrane using standard techniques. Immunoblots were incubated with indicated primary antibodies and developed using Western Lightning Plus-ECL (PerkinElmer) and imaged on an autoradiographic film or using a Bio-Rad Gel Doc system.

Co-immunoprecipitation

Serum was diluted 1:1 with PBS containing 0.02% Tween-20 (PBS-T) and incubated with α -FLAG M2 beads (Sigma) overnight at 4°C. Following wash with PBS-T, bound proteins were eluted by heating the beads at 70°C in Laemmli buffer containing 50 mM glycine buffer pH 2.8 and 9% (v/v) β -mercaptoethanol.

Adenovirus production and purification

Adenoviral vectors were created using the AdEasy system (Luo et al., 2007). C-terminally 3xFLAG-tagged murine LRG1 was cloned into pAdTrack-CMV (AddGene) linearized with XhoI (NEB) and HindIII (NEB) using In-Fusion® HD Cloning Kit (Takara). pAdTrack-CMV and pAdTrack-CMV-LRG1-FL plasmids were linearized with PmeI (NEB) and recombined into pAdEasy-1 vector via electrophoretic transformation of recombination-competent BJ5183-AD-1 cells (Agilent) with the linearized product and selection for kanamycin-resistant clones. Plasmids from validated clones were transformed into recombination-deficient XL-10 Gold ultracompetent cells (Agilent), which were used to generate pAd-eGFP and pAd-LRG1-FL plasmids and purified using Plasmid Maxi Kit (Qiagen).

Crude adenovirus was produced by transfecting PacI (NEB)-linearized pAd vectors into HEK293A cells (Invitrogen), which were incubated at 37°C with 5% CO₂ for 10-14 days with media supplementation every 3-5 days until most cells showed cytopathic effect/detachment. Both cells and the culture medium were collected, lysed by 3 cycles of freeze-thaw between dry ice-ethanol and room-temperature water baths, and centrifuged at 3500 \times g for 15 min at 4°C to obtain the supernatant crude virus. Round 1 amplification product was obtained by transducing HEK293A cells with the crude virus and repeating the above collection, lysis, and centrifugation steps.

To obtain round 2 amplification product, twelve 15 cm plates of HEK293A cells were transduced with round 1 adenovirus and incubated at 37°C with 5% CO₂ until most cells demonstrated cytopathic effect. As with previous rounds, cells and media were collected, lysed by freeze-thaw cycles, and centrifuged to obtain the supernatant. The supernatant was treated with benzonase, and adenoviral particles were purified from the crude mixture using the Vivapure AdenoPACK 100 kit (Sartorius). Purified virus was dialyzed with buffer containing 20 mM Tris pH 8, 25 mM NaCl, and 2.5% (w/v) glycerol and concentrated

using a 100 kDa centrifugal filter unit provided with the kit. Titer of the adenovirus was determined using Adeno-X Rapid Titer Kit (Takara).

AAV8 vector preparation

C-terminally 3xFLAG-tagged LRG1 was cloned into pENN.AAV.CB7.Cl.eGFP.WPRE.rBG (Addgene) linearized with EcoRI (NEB) and BglII (NEB) using In-Fusion® HD Cloning Kit (Takara). The original eGFP-expressing and cloned LRG1-FL plasmids were transformed into Stable Competent *E. coli* (NEB), purified using Plasmid Maxi Kit (Qiagen), and shipped to Penn Vector Core (PA, USA) for AAV8 production.

***In vivo* adenovirus/AAV8 transduction**

In vivo adenoviral transduction studies were performed using purified adenovirus from second round of amplification. Adenovirus was injected at a dose of 10^{10} pfu/mouse. AAV8 was injected at 10^{11} GC/mouse. The mice were briefly anesthetized with isoflurane for virus injection via the retroorbital route. Following injection, the mice were quarantined in an ABSL-2 housing room for 72 h before transferred back to regular housing conditions.

H&E section preparation/CLS quantification

Dissected tissues were fixed in 10% neutral buffered formalin for 3 days at room temperature and transferred to 70% ethanol. Paraffin embedding, sectioning, and H&E staining was performed by the Memorial Sloan Kettering Cancer Center Laboratory of Comparative Pathology. The slides were imaged using a wide-field fluorescence/brightfield/DIC microscope (Zeiss) at the Rockefeller University Bioimaging Resource Center. Crown-like structures (CLS) were identified as any adipocyte in a field of view with cellular infiltrates indicated by nuclear staining surrounding a majority of adipocyte perimeter. Objectives were used as indicated and chosen based on CLS enumerability (<30 CLS per field). 5 fields from 3 animals were quantified per group.

Multiplex cytokine panel

Mouse serum samples were diluted 1:1 with PBS, snap frozen using liquid N₂ and shipped to Eve Technologies (Alberta, Canada) on dry ice. The Mouse Cytokine Array / Chemokine Array 31-Plex (MD31) panel was used to quantify the levels of cytokines and chemokines

Cytochrome *c* clearance assay

12-week-old chow-fed LRG1-KO and WT littermate males were injected retro-orbitally with 40 mg/kg equine cytochrome *c* (Cyt *c*) in PBS. Blood was collected from the tail vein immediately prior to injection (0 min) and 5 min, 15 min, 30 min, 1 h, 2 h, 4 h, and 6 h post-injection into EDTA-coated capillary tubes and kept in ice until further processing. During blood collection, each mouse was placed on a metal grating above a clean plastic wrap to allow collection of excreted urine, if any. Plasma was isolated via centrifugation at 2000×g for 15 min at 4°C. Immunoblot against Cyt *c* was performed with WT and KO

plasma samples run pairwise to enable relative quantification of Cyt *c* signal. Quantification was performed using ImageJ (Schneider et al., 2012).

Statistical analysis

Unless otherwise noted, data are presented as mean \pm SEM, with *n* number specified in the figure legends. Statistical analyses were performed with GraphPad Prism 9. Binary comparisons were performed with Welch's *t*-test to account for possible difference in variance. Statistical analysis of data involving 3 or more conditions (levels) of a single variable was performed using one-way ANOVA followed by Dunnett post hoc tests to compare every mean with a control mean. Data measured across multiple time points as in GTT and ITT were analyzed with repeated measures two-way ANOVA, reporting group factor *P*-values. Analysis of data from a two-factor experimental setup was performed with two-way ANOVA or two-way mixed effects ANOVA in the case of an uneven *n* number, reporting group factor *P*-values. For post hoc tests, Tukey method was used when comparing every mean with every other mean and Šídák method was employed when a selected set of means were compared.

Declarations

ACKNOWLEDGEMENTS

We thank Jeffrey M. Friedman, James C. Lo, Howard C. Hang, Jingyi Chi, and Kaja Plucińska for feedback and discussions. We also thank Chingwen Yang of the CRISPR and Genome Editing Center at the Rockefeller University for generating the LRG1-KO line. We are grateful to Tao Tong and Alison North of the Bio-Imaging Resource Center at the Rockefeller University for assistance with microscopy. C.H.J.C. and S.K.S. were supported by a Medical Scientist Training Program grant from the National Institute of General Medical Sciences of the National Institutes of Health under award number T32GM007739 to the Weill Cornell/Rockefeller/Sloan Kettering Tri-Institutional MD-PhD Program. P.C. is supported by the American Diabetes Association Pathway to Stop Diabetes Grant 1-17-ACE-17. Data was generated by the Proteomics Resource Center at The Rockefeller University (RRID:SCR_017797) using instrumentation funded by the Sohn Conferences Foundation and the Leona M. and Harry B. Helmsley Charitable Trust. Bio-Render was used to make the schematic diagrams. The content of this study is solely the responsibility of the authors and does not necessarily represent the official views of the National Institutes of Health.

AUTHOR CONTRIBUTIONS

P.C. and C.H.J.C. conceived the project and designed the experiments. P.C. supervised the research. C.H.J.C., W.B., M.K., Z.L., S.K.S., A.C., and H.M. performed the experiments and analyzed the data. A.P. and T.S.C. analyzed the data. C.H.J.C. and P.C. wrote the manuscript with contributions from all authors.

COMPETING INTERESTS

The authors declare no competing interests.

DATA AVAILABILITY

The data that support the findings of this study are available from the corresponding author upon request. Reagents including unique biological materials are available from the corresponding author upon request. Proteomic and RNA-Seq data will be deposited to a public repository with accession codes available before publication.

CODE AVAILABILITY

Publicly available codes are available in the relevant references. Custom script is available upon request.

References

1. Adachi, N., Hirota, M., Hamaguchi, M., Okamoto, K., Watanabe, K., Endo, F., 2004. Serum cytochrome c level as a prognostic indicator in patients with systemic inflammatory response syndrome. *Clinica Chimica Acta* 342, 127–136. <https://doi.org/10.1016/j.cccn.2003.12.011>
2. Alleyne, T., Joseph, J., Sampson, V., 2001. Cytochrome- c Detection: A Diagnostic Marker for Myocardial Infarction. *ABAB* 90, 97–106. <https://doi.org/10.1385/ABAB:90:2:97>
3. Almagro Armenteros, J.J., Sønderby, C.K., Sønderby, S.K., Nielsen, H., Winther, O., 2017. DeepLoc: prediction of protein subcellular localization using deep learning. *Bioinformatics* 33, 3387–3395. <https://doi.org/10.1093/bioinformatics/btx431>
4. Almagro Armenteros, J.J., Tsirigos, K.D., Sønderby, C.K., Petersen, T.N., Winther, O., Brunak, S., von Heijne, G., Nielsen, H., 2019. SignalP 5.0 improves signal peptide predictions using deep neural networks. *Nature Biotechnology* 37, 420–423. <https://doi.org/10.1038/s41587-019-0036-z>
5. Alvarez-Castelao, B., Schanzenbächer, C.T., Hanus, C., Glock, C., tom Dieck, S., Dörrbaum, A.R., Bartnik, I., Nassim-Assir, B., Ciirdaeva, E., Mueller, A., Dieterich, D.C., Tirrell, D.A., Langer, J.D., Schuman, E.M., 2017. Cell-type-specific metabolic labeling of nascent proteomes in vivo. *Nature Biotechnology* 35, 1196–1201. <https://doi.org/10.1038/nbt.4016>
6. Angelantonio, E.D., Bhupathiraju, S.N., Wormser, D., Gao, P., Kaptoge, S., Gonzalez, A.B. de, Cairns, B.J., Huxley, R., Jackson, C.L., Joshy, G., Lewington, S., Manson, J.E., Murphy, N., Patel, A.V., Samet, J.M., Woodward, M., Zheng, W., Zhou, M., Bansal, N., Barricarte, A., Carter, B., Cerhan, J.R., Collins, R., Smith, G.D., Fang, X., Franco, O.H., Green, J., Halsey, J., Hildebrand, J.S., Jung, K.J., Korda, R.J., McLerran, D.F., Moore, S.C., O’Keeffe, L.M., Paige, E., Ramond, A., Reeves, G.K., Rolland, B., Sacerdote, C., Sattar, N., Sofianopoulou, E., Stevens, J., Thun, M., Ueshima, H., Yang, L., Yun, Y.D., Willeit, P., Banks, E., Beral, V., Chen, Z., Gapstur, S.M., Gunter, M.J., Hartge, P., Jee, S.H., Lam, T.-H., Peto, R., Potter, J.D., Willett, W.C., Thompson, S.G., Danesh, J., Hu, F.B., 2016. Body-mass index and all-cause mortality: individual-participant-data meta-analysis of 239 prospective studies in four continents. *The Lancet* 388, 776–786. [https://doi.org/10.1016/S0140-6736\(16\)30175-1](https://doi.org/10.1016/S0140-6736(16)30175-1)

7. Barczyk, K., Kreuter, M., Pryjma, J., Booy, E.P., Maddika, S., Ghavami, S., Berdel, W.E., Roth, J., Los, M., 2005. Serum cytochrome c indicates in vivo apoptosis and can serve as a prognostic marker during cancer therapy. *International Journal of Cancer* 116, 167–173. <https://doi.org/10.1002/ijc.21037>
8. Becher, T., Palanisamy, S., Kramer, D.J., Eljalby, M., Marx, S.J., Wibmer, A.G., Butler, S.D., Jiang, C.S., Vaughan, R., Schöder, H., Mark, A., Cohen, P., 2021. Brown adipose tissue is associated with cardiometabolic health. *Nature Medicine* 27, 58–65. <https://doi.org/10.1038/s41591-020-1126-7>
9. Ben-Ari, Z., Schmilovotz-Weiss, H., Belinki, A., Pappo, O., Sulkes, J., Neuman, M.G., Kaganovsky, E., Kfir, B., Tur-Kaspa, R., Klein, T., 2003. Circulating soluble cytochrome c in liver disease as a marker of apoptosis. *Journal of Internal Medicine* 254, 168–175. <https://doi.org/10.1046/j.1365-2796.2003.01171.x>
10. Belczacka, I., Latosinska, A., Metzger, J., Marx, D., Vlahou, A., Mischak, H., Frantzi, M., 2019. Proteomics biomarkers for solid tumors: Current status and future prospects. *Mass Spectrometry Reviews* 38, 49–78. <https://doi.org/10.1002/mas.21572>
11. Bendtsen, J.D., Jensen, L.J., Blom, N., von Heijne, G., Brunak, S., 2004. Feature-based prediction of non-classical and leaderless protein secretion. *Protein Engineering, Design and Selection* 17, 349–356. <https://doi.org/10.1093/protein/gzh037>
12. Branon, T.C., Bosch, J.A., Sanchez, A.D., Udeshi, N.D., Svinkina, T., Carr, S.A., Feldman, J.L., Perrimon, N., Ting, A.Y., 2018. Efficient proximity labeling in living cells and organisms with TurboID. *Nature Biotechnology* 36, 880–887. <https://doi.org/10.1038/nbt.4201>
13. Calve, S., Witten, A.J., Ocken, A.R., Kinzer-Ursem, T.L., 2016. Incorporation of non-canonical amino acids into the developing murine proteome. *Scientific Reports* 6, 32377. <https://doi.org/10.1038/srep32377>
14. Chen, Z., Huang, A., Sun, J., Jiang, T., Qin, F.X.-F., Wu, A., 2017. Inference of immune cell composition on the expression profiles of mouse tissue. *Scientific Reports* 7, 40508. <https://doi.org/10.1038/srep40508>
15. Chi, J., Wu, Z., Choi, C.H.J., Nguyen, L., Tegegne, S., Ackerman, S.E., Crane, A., Marchildon, F., Tessier-Lavigne, M., Cohen, P., 2018. Three-Dimensional Adipose Tissue Imaging Reveals Regional Variation in Beige Fat Biogenesis and PRDM16-Dependent Sympathetic Neurite Density. *Cell Metabolism* 27, 226-236.e3. <https://doi.org/10.1016/j.cmet.2017.12.011>
16. Chi, J., Lin, Z., Barr, W., Crane, A., Zhu, X.G., Cohen, P., 2021. Early postnatal interactions between beige adipocytes and sympathetic neurites regulate innervation of subcutaneous fat. *eLife* 10, e64693. <https://doi.org/10.7554/eLife.64693>
17. Chouchani, E.T., Kazak, L., Spiegelman, B.M., 2019. New Advances in Adaptive Thermogenesis: UCP1 and Beyond. *Cell Metabolism* 29, 27–37. <https://doi.org/10.1016/j.cmet.2018.11.002>
18. Cinti, S., Mitchell, G., Barbatelli, G., Murano, I., Ceresi, E., Faloia, E., Wang, S., Fortier, M., Greenberg, A.S., Obin, M.S., 2005. Adipocyte death defines macrophage localization and function in adipose tissue of obese mice and humans. *Journal of Lipid Research* 46, 2347–2355. <https://doi.org/10.1194/jlr.M500294-JLR200>

19. Concordet, J.-P., Haeussler, M., 2018. CRISPOR: intuitive guide selection for CRISPR/Cas9 genome editing experiments and screens. *Nucleic Acids Research* 46, W242–W245.
<https://doi.org/10.1093/nar/gky354>
20. Cox, J., Hein, M.Y., Lubner, C.A., Paron, I., Nagaraj, N., Mann, M., 2014. Accurate Proteome-wide Label-free Quantification by Delayed Normalization and Maximal Peptide Ratio Extraction, Termed MaxLFQ *. *Molecular & Cellular Proteomics* 13, 2513–2526.
<https://doi.org/10.1074/mcp.M113.031591>
21. Cummings, C., Walder, J., Treeful, A., Jemmerson, R., 2006. Serum leucine-rich alpha-2-glycoprotein-1 binds cytochrome c and inhibits antibody detection of this apoptotic marker in enzyme-linked immunosorbent assay. *Apoptosis* 11, 1121–1129. <https://doi.org/10.1007/s10495-006-8159-3>
22. Davis, C.A., Hitz, B.C., Sloan, C.A., Chan, E.T., Davidson, J.M., Gabdank, I., Hilton, J.A., Jain, K., Baymuradov, U.K., Narayanan, A.K., Onate, K.C., Graham, K., Miyasato, S.R., Dreszer, T.R., Strattan, J.S., Jolanki, O., Tanaka, F.Y., Cherry, J.M., 2018. The Encyclopedia of DNA elements (ENCODE): data portal update. *Nucleic Acids Research* 46, D794–D801. <https://doi.org/10.1093/nar/gkx1081>
23. Dieterich, D.C., Link, A.J., Graumann, J., Tirrell, D.A., Schuman, E.M., 2006. Selective identification of newly synthesized proteins in mammalian cells using bioorthogonal noncanonical amino acid tagging (BONCAT). *PNAS* 103, 9482–9487. <https://doi.org/10.1073/pnas.0601637103>
24. Eichelbaum, K., Winter, M., Diaz, M.B., Herzig, S., Krijgsvelde, J., 2012. Selective enrichment of newly synthesized proteins for quantitative secretome analysis. *Nat Biotech* 30, 984–990.
<https://doi.org/10.1038/nbt.2356>
25. Eichelbaum, K., Krijgsvelde, J., 2014. Combining Pulsed SILAC Labeling and Click-Chemistry for Quantitative Secretome Analysis, in: Ivanov, A.I. (Ed.), *Exocytosis and Endocytosis, Methods in Molecular Biology*. Springer New York, pp. 101–114. https://doi.org/10.1007/978-1-4939-0944-5_7
26. Farrell, G., Schattenberg, J.M., Leclercq, I., Yeh, M.M., Goldin, R., Teoh, N., Schuppan, D., 2019. Mouse Models of Nonalcoholic Steatohepatitis: Toward Optimization of Their Relevance to Human Nonalcoholic Steatohepatitis. *Hepatology* 69, 2241–2257. <https://doi.org/10.1002/hep.30333>
27. Feldstein, A.E., Canbay, A., Angulo, P., Taniai, M., Burgart, L.J., Lindor, K.D., Gores, G.J., 2003. Hepatocyte apoptosis and fas expression are prominent features of human nonalcoholic steatohepatitis. *Gastroenterology* 125, 437–443. [https://doi.org/10.1016/S0016-5085\(03\)00907-7](https://doi.org/10.1016/S0016-5085(03)00907-7)
28. Fox C.S., Massaro J.M., Hoffmann U., Pou K.M., Maurovich-Horvat P, Liu C.-Y., Vasan R.S., Murabito J.M., Meigs J.B., Cupples L.A., D’Agostino R.B., O’Donnell C.J., 2007. Abdominal Visceral and Subcutaneous Adipose Tissue Compartments. *Circulation* 116, 39–48.
<https://doi.org/10.1161/CIRCULATIONAHA.106.675355>
29. Funcke, J.-B., Scherer, P.E., 2019. Beyond adiponectin and leptin: adipose tissue-derived mediators of inter-organ communication. *Journal of Lipid Research* 60, 1648–1697.
<https://doi.org/10.1194/jlr.R094060>
30. Gómez-Banoy, N., Guseh, J.S., Li, G., Rubio-Navarro, A., Chen, T., Poirier, B., Putzel, G., Rosselot, C., Pabón, M.A., Camporez, J.P., Bhambhani, V., Hwang, S.-J., Yao, C., Perry, R.J., Mukherjee, S., Larson,

- M.G., Levy, D., Dow, L.E., Shulman, G.I., Dephore, N., Garcia-Ocana, A., Hao, M., Spiegelman, B.M., Ho, J.E., Lo, J.C., 2019. Adipsin preserves beta cells in diabetic mice and associates with protection from type 2 diabetes in humans. *Nature Medicine* 25, 1739–1747. <https://doi.org/10.1038/s41591-019-0610-4>
31. Grazioli, S., Pugin, J., 2018. Mitochondrial Damage-Associated Molecular Patterns: From Inflammatory Signaling to Human Diseases. *Front. Immunol.* 9. <https://doi.org/10.3389/fimmu.2018.00832>
32. Hotamisligil, G.S., Bernlohr, D.A., 2015. Metabolic functions of FABPs—mechanisms and therapeutic implications. *Nature Reviews Endocrinology* 11, 592–605. <https://doi.org/10.1038/nrendo.2015.122>
33. Huang, D.W., Sherman, B.T., Lempicki, R.A., 2009a. Systematic and integrative analysis of large gene lists using DAVID bioinformatics resources. *Nature Protocols* 4, 44–57. <https://doi.org/10.1038/nprot.2008.211>
34. Jemmerson, R., LaPlante, B., Treeful, A., 2002. Release of intact, monomeric cytochrome c from apoptotic and necrotic cells. *Cell Death and Differentiation* 9, 538–548. <https://doi.org/10.1038/sj.cdd.4400981>
35. Kentsis, A., Lin, Y.Y., Kurek, K., Calicchio, M., Wang, Y.Y., Monigatti, F., Campagne, F., Lee, R., Horwitz, B., Steen, H., Bachur, R., 2010. Discovery and Validation of Urine Markers of Acute Pediatric Appendicitis Using High-Accuracy Mass Spectrometry. *Annals of Emergency Medicine* 55, 62-70.e4. <https://doi.org/10.1016/j.annemergmed.2009.04.020>
36. Kleinert, M., Clemmensen, C., Hofmann, S.M., Moore, M.C., Renner, S., Woods, S.C., Huypens, P., Beckers, J., de Angelis, M.H., Schürmann, A., Bakhti, M., Klingenspor, M., Heiman, M., Cherrington, A.D., Ristow, M., Lickert, H., Wolf, E., Havel, P.J., Müller, T.D., Tschöp, M.H., 2018. Animal models of obesity and diabetes mellitus. *Nature Reviews Endocrinology* 14, 140–162. <https://doi.org/10.1038/nrendo.2017.161>
37. Krogh, A., Larsson, B., von Heijne, G., Sonnhammer, E.L.L., 2001. Predicting transmembrane protein topology with a hidden markov model: application to complete genomes¹¹ Edited by F. Cohen. *Journal of Molecular Biology* 305, 567–580. <https://doi.org/10.1006/jmbi.2000.4315>
38. Lackey, D.E., Olefsky, J.M., 2016. Regulation of metabolism by the innate immune system. *Nature Reviews Endocrinology* 12, 15–28. <https://doi.org/10.1038/nrendo.2015.189>
39. Lee, P., Smith, S., Linderman, J., Courville, A.B., Brychta, R.J., Dieckmann, W., Werner, C.D., Chen, K.Y., Celi, F.S., 2014. Temperature-Acclimated Brown Adipose Tissue Modulates Insulin Sensitivity in Humans. *Diabetes* 63, 3686–3698. <https://doi.org/10.2337/db14-0513>
40. Lo, J.C., Ljubicic, S., Leibiger, B., Kern, M., Leibiger, I.B., Moede, T., Kelly, M.E., Chatterjee Bhowmick, D., Murano, I., Cohen, P., Banks, A.S., Khandekar, M.J., Dietrich, A., Flier, J.S., Cinti, S., Blüher, M., Danial, N.N., Berggren, P.-O., Spiegelman, B.M., 2014. Adipsin Is an Adipokine that Improves β Cell Function in Diabetes. *Cell* 158, 41–53. <https://doi.org/10.1016/j.cell.2014.06.005>
41. Love, M.I., Huber, W., Anders, S., 2014. Moderated estimation of fold change and dispersion for RNA-seq data with DESeq2. *Genome Biology* 15, 550. <https://doi.org/10.1186/s13059-014-0550-8>

42. Luo, J., Deng, Z.-L., Luo, X., Tang, N., Song, W.-X., Chen, J., Sharff, K.A., Luu, H.H., Haydon, R.C., Kinzler, K.W., Vogelstein, B., He, T.-C., 2007. A protocol for rapid generation of recombinant adenoviruses using the AdEasy system. *Nat. Protocols* 2, 1236–1247. <https://doi.org/10.1038/nprot.2007.135>
43. McClatchy, D.B., Ma, Y., Liu, C., Stein, B.D., Martínez-Bartolomé, S., Vasquez, D., Hellberg, K., Shaw, R.J., Yates, J.R., 2015. Pulsed Azidohomoalanine Labeling in Mammals (PALM) Detects Changes in Liver-Specific LKB1 Knockout Mice. *J. Proteome Res.* 14, 4815–4822. <https://doi.org/10.1021/acs.jproteome.5b00653>
44. Naka, T., Fujimoto, M., 2018. LRG is a novel inflammatory marker clinically useful for the evaluation of disease activity in rheumatoid arthritis and inflammatory bowel disease. *Immunological Medicine* 41, 62–67. <https://doi.org/10.1080/13497413.2018.1481582>
45. Newman, A.M., Steen, C.B., Liu, C.L., Gentles, A.J., Chaudhuri, A.A., Scherer, F., Khodadoust, M.S., Esfahani, M.S., Luca, B.A., Steiner, D., Diehn, M., Alizadeh, A.A., 2019. Determining cell type abundance and expression from bulk tissues with digital cytometry. *Nature Biotechnology* 37, 773–782. <https://doi.org/10.1038/s41587-019-0114-2>
46. Oh, D.Y., Morinaga, H., Talukdar, S., Bae, E.J., Olefsky, J.M., 2012. Increased Macrophage Migration Into Adipose Tissue in Obese Mice. *Diabetes* 61, 346–354. <https://doi.org/10.2337/db11-0860>
47. Pek, S.L.T., Cheng, A.K.S., Lin, M.X., Wong, M.S., Chan, E.Z.L., Moh, A.M.C., Sum, C.F., Lim, S.C., Tavintharan, S., 2018. Association of circulating proinflammatory marker, leucine-rich- α 2-glycoprotein (LRG1), following metabolic/bariatric surgery. *Diabetes/Metabolism Research and Reviews* 34, e3029. <https://doi.org/10.1002/dmrr.3029>
48. Peyrou, M., Cereijo, R., Quesada-López, T., Campderrós, L., Gavaldà-Navarro, A., Liñares-Pose, L., Kaschina, E., Unger, T., López, M., Giralt, M., Villarroya, F., 2020. The kallikrein–kinin pathway as a mechanism for auto-control of brown adipose tissue activity. *Nature Communications* 11, 2132. <https://doi.org/10.1038/s41467-020-16009-x>
49. Pierleoni, A., Martelli, P.L., Casadio, R., 2008. PredGPI: a GPI-anchor predictor. *BMC Bioinformatics* 9, 392. <https://doi.org/10.1186/1471-2105-9-392>
50. Pirkmajer, S., Chibalin, A.V., 2011. Serum starvation: caveat emptor. *American Journal of Physiology-Cell Physiology* 301, C272–C279. <https://doi.org/10.1152/ajpcell.00091.2011>
51. Pullerits, R., Bokarewa, M., Jonsson, I.-M., Verdrengh, M., Tarkowski, A., 2005. Extracellular cytochrome c, a mitochondrial apoptosis-related protein, induces arthritis. *Rheumatology (Oxford)* 44, 32–39. <https://doi.org/10.1093/rheumatology/keh406>
52. Radhakrishnan, J., Wang, S., Ayoub, I.M., Kolarova, J.D., Levine, R.F., Gazmuri, R.J., 2007. Circulating levels of cytochrome c after resuscitation from cardiac arrest: a marker of mitochondrial injury and predictor of survival. *American Journal of Physiology-Heart and Circulatory Physiology* 292, H767–H775. <https://doi.org/10.1152/ajpheart.00468.2006>
53. Rappsilber, J., Mann, M., Ishihama, Y., 2007. Protocol for micro-purification, enrichment, pre-fractionation and storage of peptides for proteomics using StageTips. *Nature Protocols* 2, 1896–1906. <https://doi.org/10.1038/nprot.2007.261>

54. Renz, A., Berdel, W.E., Kreuter, M., Belka, C., Schulze-Osthoff, K., Los, M., 2001. Rapid extracellular release of cytochrome c is specific for apoptosis and marks cell death in vivo. *Blood* 98, 1542–1548. <https://doi.org/10.1182/blood.V98.5.1542>
55. Ritchie, M.E., Phipson, B., Wu, D., Hu, Y., Law, C.W., Shi, W., Smyth, G.K., 2015. limma powers differential expression analyses for RNA-sequencing and microarray studies. *Nucleic Acids Research* 43, e47–e47. <https://doi.org/10.1093/nar/gkv007>
56. Rosen, E.D., Spiegelman, B.M., 2014. What We Talk About When We Talk About Fat. *Cell* 156, 20–44. <https://doi.org/10.1016/j.cell.2013.12.012>
57. Saltiel, A.R., Olefsky, J.M., 2017. Inflammatory mechanisms linking obesity and metabolic disease. *J Clin Invest* 127, 1–4. <https://doi.org/10.1172/JCI92035>
58. Schneider, C.A., Rasband, W.S., Eliceiri, K.W., 2012. NIH Image to ImageJ: 25 years of image analysis. *Nature Methods* 9, 671–675. <https://doi.org/10.1038/nmeth.2089>
59. Shin, J.-B., Krey, J.F., Hassan, A., Metlagel, Z., Tauscher, A.N., Pagana, J.M., Sherman, N.E., Jeffery, E.D., Spinelli, K.J., Zhao, H., Wilmarth, P.A., Choi, D., David, L.L., Auer, M., Barr-Gillespie, P.G., 2013. Molecular architecture of the chick vestibular hair bundle. *Nature Neuroscience* 16, 365–374. <https://doi.org/10.1038/nn.3312>
60. Shola, D.T.N., Yang, C., Han, C., Norinsky, R., Peraza, R.D., 2021. Generation of Mouse Model (KI and CKO) via Easi-CRISPR, in: Singh, S.R., Hoffman, R.M., Singh, A. (Eds.), *Mouse Genetics: Methods and Protocols, Methods in Molecular Biology*. Springer US, New York, NY, pp. 1–27. https://doi.org/10.1007/978-1-0716-1008-4_1
61. Su, A.I., Wiltshire, T., Batalov, S., Lapp, H., Ching, K.A., Block, D., Zhang, J., Soden, R., Hayakawa, M., Kreiman, G., Cooke, M.P., Walker, J.R., Hogenesch, J.B., 2004. A gene atlas of the mouse and human protein-encoding transcriptomes. *PNAS* 101, 6062–6067. <https://doi.org/10.1073/pnas.0400782101>
62. Svensson, K.J., Long, J.Z., Jedrychowski, M.P., Cohen, P., Lo, J.C., Serag, S., Kir, S., Shinoda, K., Tartaglia, J.A., Rao, R.R., Chédotal, A., Kajimura, S., Gygi, S.P., Spiegelman, B.M., 2016. A Secreted Slit2 Fragment Regulates Adipose Tissue Thermogenesis and Metabolic Function. *Cell Metabolism* 23, 454–466. <https://doi.org/10.1016/j.cmet.2016.01.008>
63. Trak-Smayra, V., Paradis, V., Massart, J., Nasser, S., Jebara, V., Fromenty, B., 2011. Pathology of the liver in obese and diabetic ob/ob and db/db mice fed a standard or high-calorie diet. *International Journal of Experimental Pathology* 92, 413–421. <https://doi.org/10.1111/j.1365-2613.2011.00793.x>
64. Tran, T.T., Yamamoto, Y., Gesta, S., Kahn, C.R., 2008. Beneficial Effects of Subcutaneous Fat Transplantation on Metabolism. *Cell Metabolism* 7, 410–420. <https://doi.org/10.1016/j.cmet.2008.04.004>
65. Tyanova, S., Temu, T., Sinitcyn, P., Carlson, A., Hein, M.Y., Geiger, T., Mann, M., Cox, J., 2016. The Perseus computational platform for comprehensive analysis of (prote)omics data. *Nature Methods* 13, 731–740. <https://doi.org/10.1038/nmeth.3901>
66. Wang, X., Abraham, S., McKenzie, J.A.G., Jeffs, N., Swire, M., Tripathi, V.B., Luhmann, U.F.O., Lange, C.A.K., Zhai, Z., Arthur, H.M., Bainbridge, J.W.B., Moss, S.E., Greenwood, J., 2013. LRG1 promotes

- angiogenesis by modulating endothelial TGF- β signalling. *Nature* 499, nature12345.
<https://doi.org/10.1038/nature12345>
67. Wang, W., Seale, P., 2016. Control of brown and beige fat development. *Nat Rev Mol Cell Biol* 17, 691–702. <https://doi.org/10.1038/nrm.2016.96>
68. Wang, Z.V., Scherer, P.E., 2016. Adiponectin, the past two decades. *Journal of Molecular Cell Biology* 8, 93–100. <https://doi.org/10.1093/jmcb/mjw011>
69. Wang, P., Loh, K.H., Wu, M., Morgan, D.A., Schneeberger, M., Yu, X., Chi, J., Kosse, C., Kim, D., Rahmouni, K., Cohen, P., Friedman, J., 2020. A leptin–BDNF pathway regulating sympathetic innervation of adipose tissue. *Nature* 583, 839–844. <https://doi.org/10.1038/s41586-020-2527-y>
70. Wei, W., Riley, N.M., Yang, A.C., Kim, J.T., Terrell, S.M., Li, V.L., Garcia-Contreras, M., Bertozzi, C.R., Long, J.Z., 2021. Cell type-selective secretome profiling in vivo. *Nature Chemical Biology* 17, 326–334. <https://doi.org/10.1038/s41589-020-00698-y>
71. Weisberg, S.P., McCann, D., Desai, M., Rosenbaum, M., Leibel, R.L., Ferrante, A.W., 2003. Obesity is associated with macrophage accumulation in adipose tissue. *J Clin Invest* 112, 1796–1808. <https://doi.org/10.1172/JCI19246>
72. Wenzel, T.J., Bajwa, E., Klegeris, A., 2019. Cytochrome c can be released into extracellular space and modulate functions of human astrocytes in a toll-like receptor 4-dependent manner. *Biochimica et Biophysica Acta (BBA) - General Subjects* 1863, 129400. <https://doi.org/10.1016/j.bbagen.2019.07.009>
73. Winzell, M.S., Ahrén, B., 2004. The High-Fat Diet–Fed Mouse: A Model for Studying Mechanisms and Treatment of Impaired Glucose Tolerance and Type 2 Diabetes. *Diabetes* 53, S215–S219. https://doi.org/10.2337/diabetes.53.suppl_3.S215
74. Wu, C., Jin, X., Tsueng, G., Afrasiabi, C., Su, A.I., 2016. BioGPS: building your own mash-up of gene annotations and expression profiles. *Nucleic Acids Research* 44, D313–D316. <https://doi.org/10.1093/nar/gkv1104>
75. Yang, Q., Graham, T.E., Mody, N., Preitner, F., Peroni, O.D., Zabolotny, J.M., Kotani, K., Quadro, L., Kahn, B.B., 2005. Serum retinol binding protein 4 contributes to insulin resistance in obesity and type 2 diabetes. *Nature* 436, 356–362. <https://doi.org/10.1038/nature03711>
76. Yu, G., Wang, L.-G., Han, Y., He, Q.-Y., 2012. clusterProfiler: an R Package for Comparing Biological Themes Among Gene Clusters. *OMICS: A Journal of Integrative Biology* 16, 284–287. <https://doi.org/10.1089/omi.2011.0118>
77. Zeng, X., Ye, M., Resch, J.M., Jedrychowski, M.P., Hu, B., Lowell, B.B., Ginty, D.D., Spiegelman, B.M., 2019. Innervation of thermogenic adipose tissue via a calyntenin 3 β –S100b axis. *Nature* 569, 229. <https://doi.org/10.1038/s41586-019-1156-9>

Figures

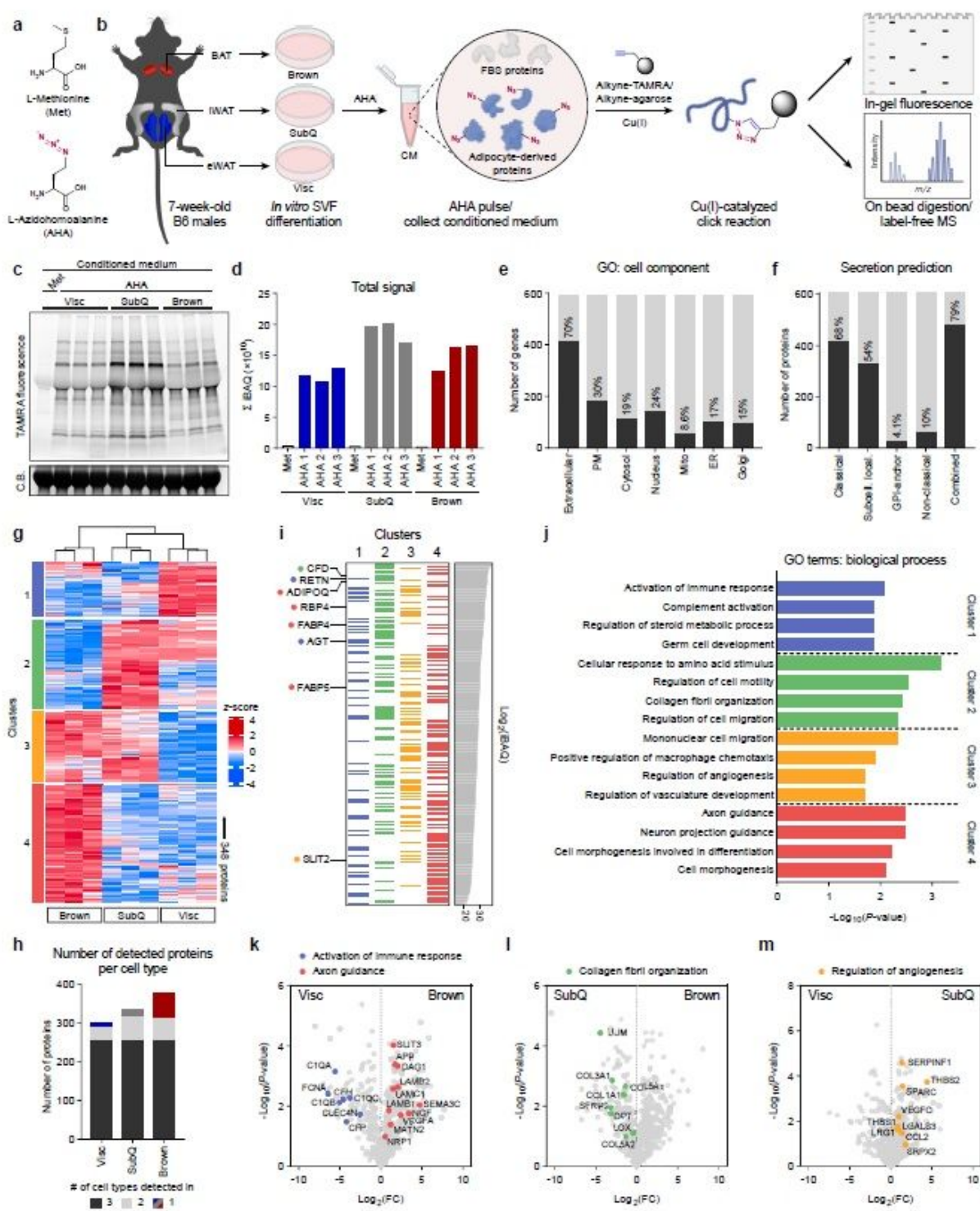


Figure 1

Characterization of primary adipocyte secretome using BONCAT a, Chemical structures of L-methionine (Met) and L-azidohomoalanine (AHA). b, Schematic diagram of MS-based secretome analysis from primary Visc, SubQ, and Brown adipocytes using BONCAT. c, In-gel fluorescence analysis of TAMRA-conjugated CM proteins from Met-pulsed (lane 1) or AHA-pulsed (lanes 2-10) adipocytes. C.B., Coomassie Blue. d, Sum of iBAQ intensities (Σ iBAQ) across all quantified proteins in each CM. e, Number and

proportion of genes annotated to GO cell component terms. Extracellular, extracellular region, space, or matrix; PM, plasma membrane; Mito, mitochondrion; ER, endoplasmic reticulum; Golgi, Golgi apparatus. f, Number and proportion of proteins predicted to be secreted by prediction algorithms. g, Heatmap of 348 differentially secreted proteins across cell types. h, Number of proteins detected in at least 2 of 3 replicates per cell type, color-coded based on number of cell types a protein is detected in. i, 348 proteins grouped in clusters from g and arranged in decreasing order of iBAQ intensities. Previously described adipokines are indicated. j, Top 4 overrepresented GO biological process terms per cluster and their enrichment scores. k-m, Pairwise comparisons of Log₂(LFQ) intensities between Visc and Brown (k), SubQ and Brown (l), and Visc and SubQ (m) CM. Proteins and their annotated pathway terms from j are indicated.

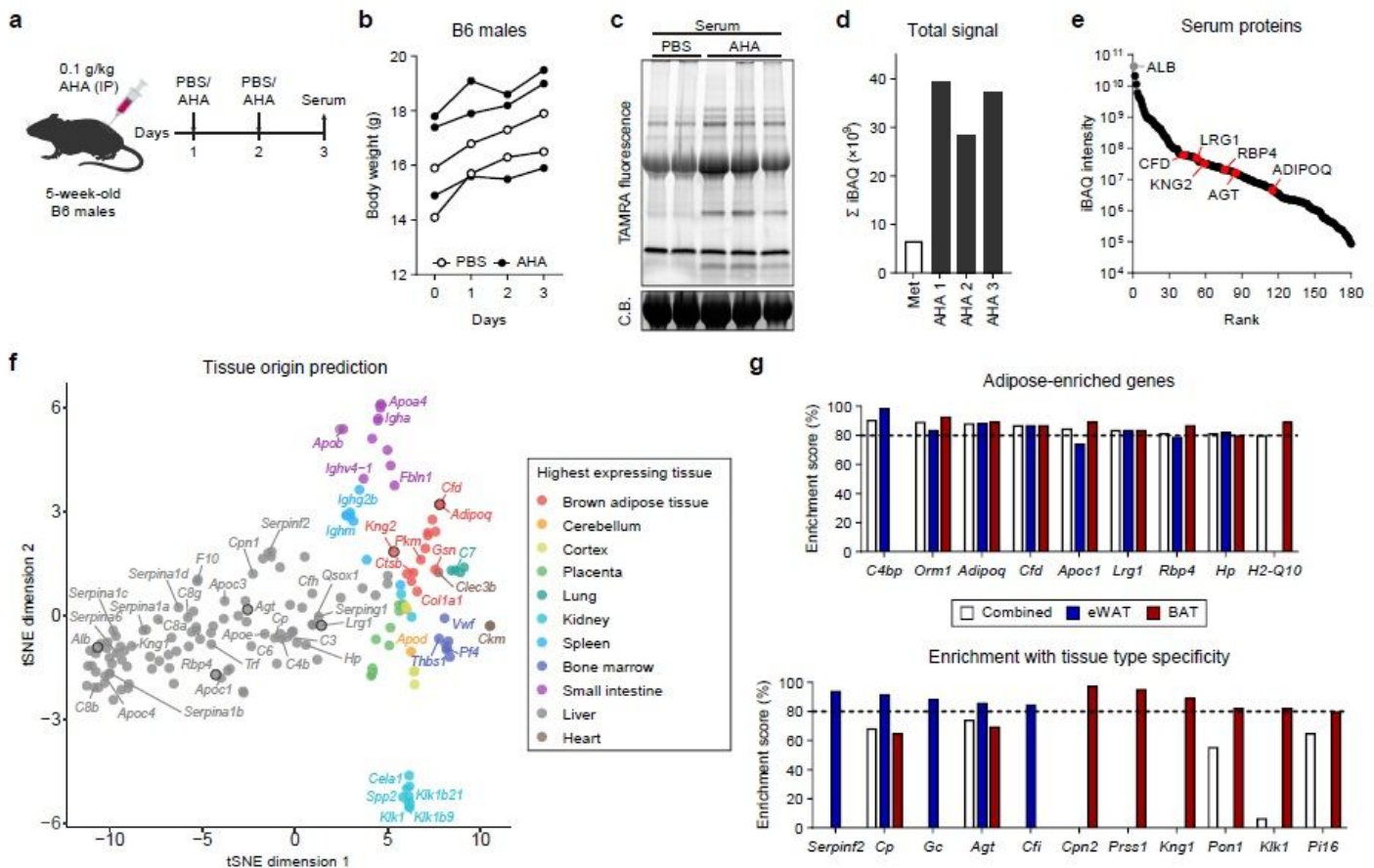


Figure 2

Profiling in vivo nascent serum proteome using BONCAT a, Schematic of AHA IP injections. b, Body weights of mice injected with PBS (n = 2) or AHA (n = 3). c, In-gel fluorescence analysis of TAMRA-conjugated serum proteins from PBS-pulsed (lanes 1 and 2) or AHA-pulsed (lanes 3-5) mice. C.B., Coomassie Blue. d, Sum of iBAQ intensities (Σ iBAQ) across all quantified proteins in each serum. e, iBAQ intensities of detected serum samples arranged in decreasing order. f, t-SNE clustering of detected serum protein genes based on tissue mRNA levels from the ENCODE/LICR dataset. g, Adipose tissue-enriched serum protein genes and % enrichment scores calculated from Bio-GPS dataset.

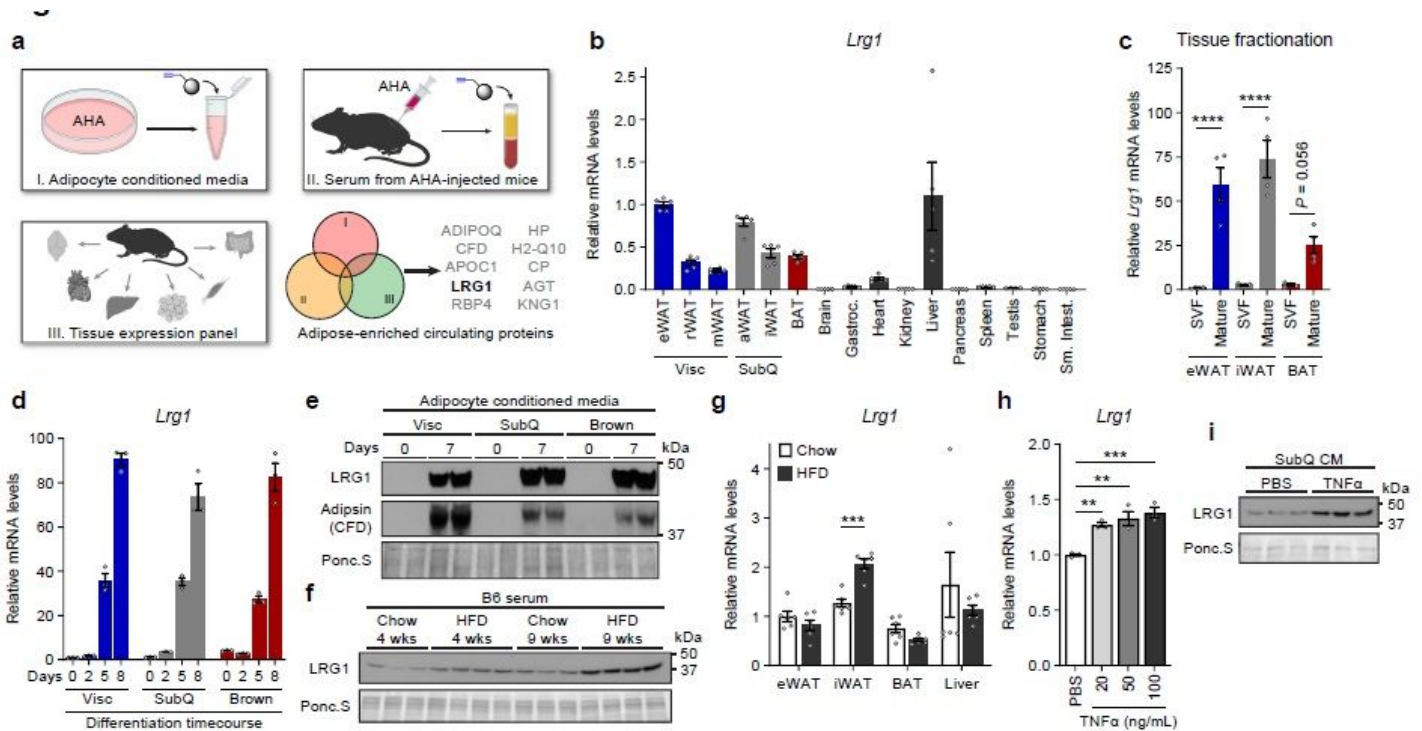


Figure 3

LRG1 is secreted by mature adipocytes and increased in obesity a, Search strategy for identification of novel adipokines with a potential role in whole-body metabolism. b, Relative *Lrg1* mRNA levels across a panel of tissues from 8-week-old male B6 mice. Visc, visceral fat depots; SubQ, subcutaneous fat depots. n = 4-5 per group. c, Relative *Lrg1* mRNA levels of indicated adipose tissues fractionated into mature adipocytes and SVF. ****P < 0.0001 from Šídák post hoc test following two-way ANOVA. n = 4 per group. d, Relative *Lrg1* mRNA levels during in vitro differentiation of primary SVF into adipocytes. n = 3 per group. e, Western blot of LRG1 and CFD in CM before (day 0) and after (day 7) in vitro adipogenic differentiation. f, Serum western blot of LRG1 from male B6 mice on standard chow or HFD for indicated weeks. HFD was started at 6 weeks of age. g, Relative *Lrg1* mRNA levels of indicated tissues from mice on standard chow or HFD for 15 weeks. HFD was started at 6 weeks of age. ***P < 0.001 from two-sided Welch's t-test. n = 6 per group. h, Relative *Lrg1* mRNA levels of primary SubQ adipocytes treated with recombinant TNFα and 850 nM insulin for 6 h. **P < 0.01, ***P < 0.001 from Dunnett post hoc test following one-way ANOVA. n = 3 per group. i, Western blot of LRG1 in CM of primary SubQ adipocytes treated with PBS or 100 ng/mL recombinant TNFα without insulin for 24 h. Data are presented as mean ± SEM.

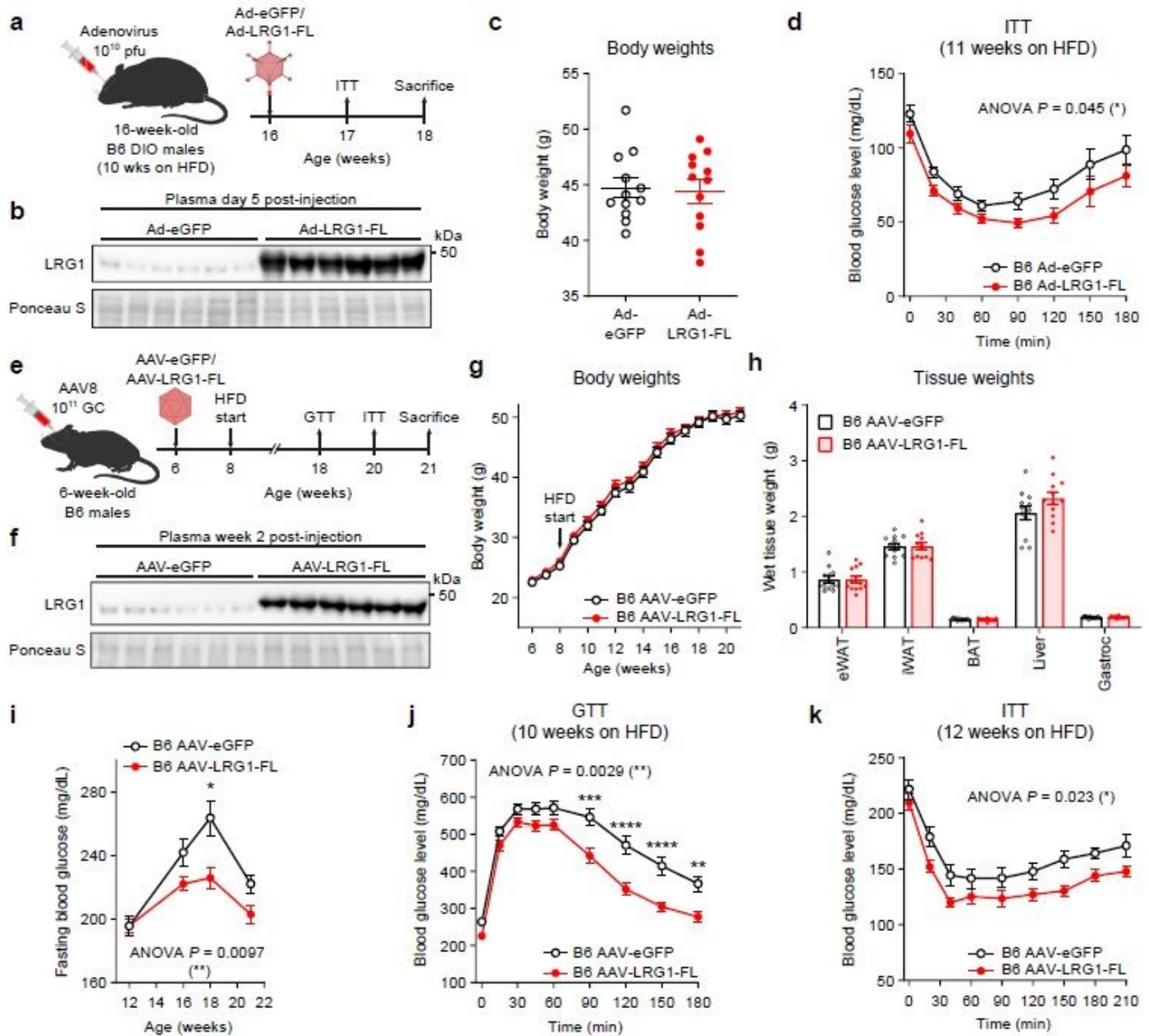


Figure 4

LRG1 overexpression improves glucose homeostasis in C57BL/6J DIO mice a, Schematic of Ad vector-mediated acute LRG1 overexpression in B6 DIO male mice. b, Plasma western blot of LRG1 5 days after Ad injection. c, Body weights of Ad-transduced B6 males at 17 weeks of age (11 weeks on HFD). d, Insulin tolerance test (1.0 U/kg) in Ad-transduced B6 males at 17 weeks of age (11 weeks on HFD). Ad cohort consisted of $n = 12$ per group. e, Schematic of AAV8-mediated chronic LRG1 overexpression in B6 males. AAV injection was performed in 6-week-old B6 males. HFD was started at 8 weeks of age. f, Plasma western blot of LRG1 2 weeks after AAV injection. g, Body weights of AAV-transduced B6 male mice during HFD challenge. h, Weights of dissected tissues from AAV-transduced B6 male mice at 21 weeks of age (13 weeks on HFD). i, 6 h fasting blood glucose levels of AAV-transduced B6 male mice during HFD feeding. j, Intraperitoneal glucose tolerance test (1.5 g/kg) in AAV-transduced B6 males at 18 weeks of

age (10 weeks on HFD). k, Insulin tolerance test (1.5 U/kg) in AAV-transduced B6 males at 20 weeks of age (12 weeks on HFD). AAV cohort consisted of $n = 12$ per group. Data are presented as mean \pm SEM. ANOVA P indicates group factor P-values from repeated measures two-way ANOVA. Where indicated, P-values from Šídák post hoc tests are reported. * $P < 0.05$, ** $P < 0.01$, *** $P < 0.001$, **** $P < 0.0001$.

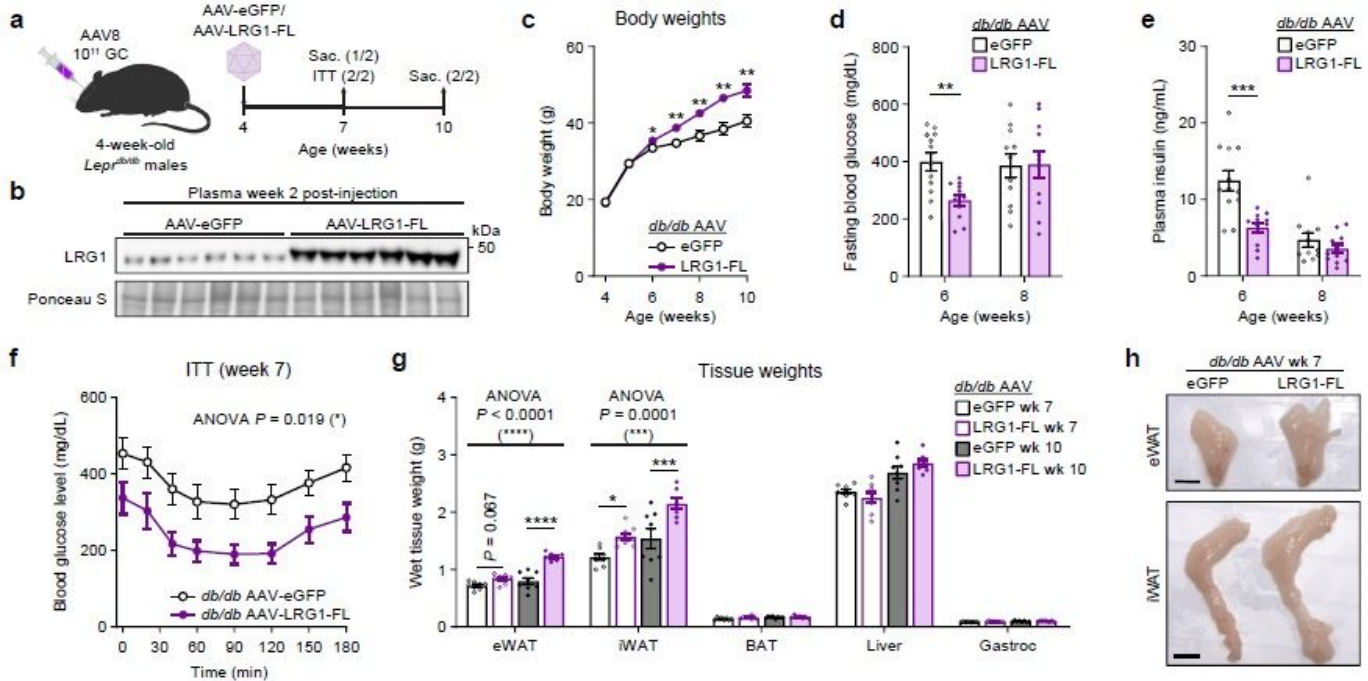


Figure 5

LRG1 overexpression in C57BLKS/J-*Lep^{rd/rd}* mice delays onset of diabetic phenotype and promotes WAT expansion a, Schematic of AAV8-mediated LRG1 overexpression in *db/db* males. b, Plasma western blot of LRG1 2 weeks after AAV injection. c, Body weights of AAV-transduced *db/db* male mice on standard chow diet. * $P < 0.05$, ** $P < 0.01$ from two-sided Welch's t-test. $n = 16$ per group for weeks 4-6; $n = 7-8$ per group for weeks 7-10. d, 6 h fasting blood glucose levels of AAV-transduced *db/db* male mice at 6 and 8 weeks of age. ** $P < 0.01$ from two-sided Welch's t-test. $n = 11-12$ per group. e, Plasma insulin levels from d. *** $P < 0.001$ from two-sided Welch's t-test. f, Insulin tolerance test (2.0 U/kg) in AAV-transduced 7-week-old *db/db* male mice. ANOVA P indicates group factor P-value from repeated measures two-way ANOVA. * $P < 0.05$. $n = 7-8$ per group. g, Weights of dissected tissues from AAV-transduced *db/db* male mice at 7 and 10 weeks of age. ANOVA P indicates group factor P-values from two-way mixed effects ANOVA. Where indicated, P-values from Šídák post hoc tests reported. * $P < 0.05$, *** $P < 0.001$, **** $P < 0.0001$. $n = 7-8$ per group. h, eWAT and iWAT of AAV-transduced *db/db* male mice at 7 weeks of age. Scale bars indicate 1 cm. Data are presented as mean \pm SEM.

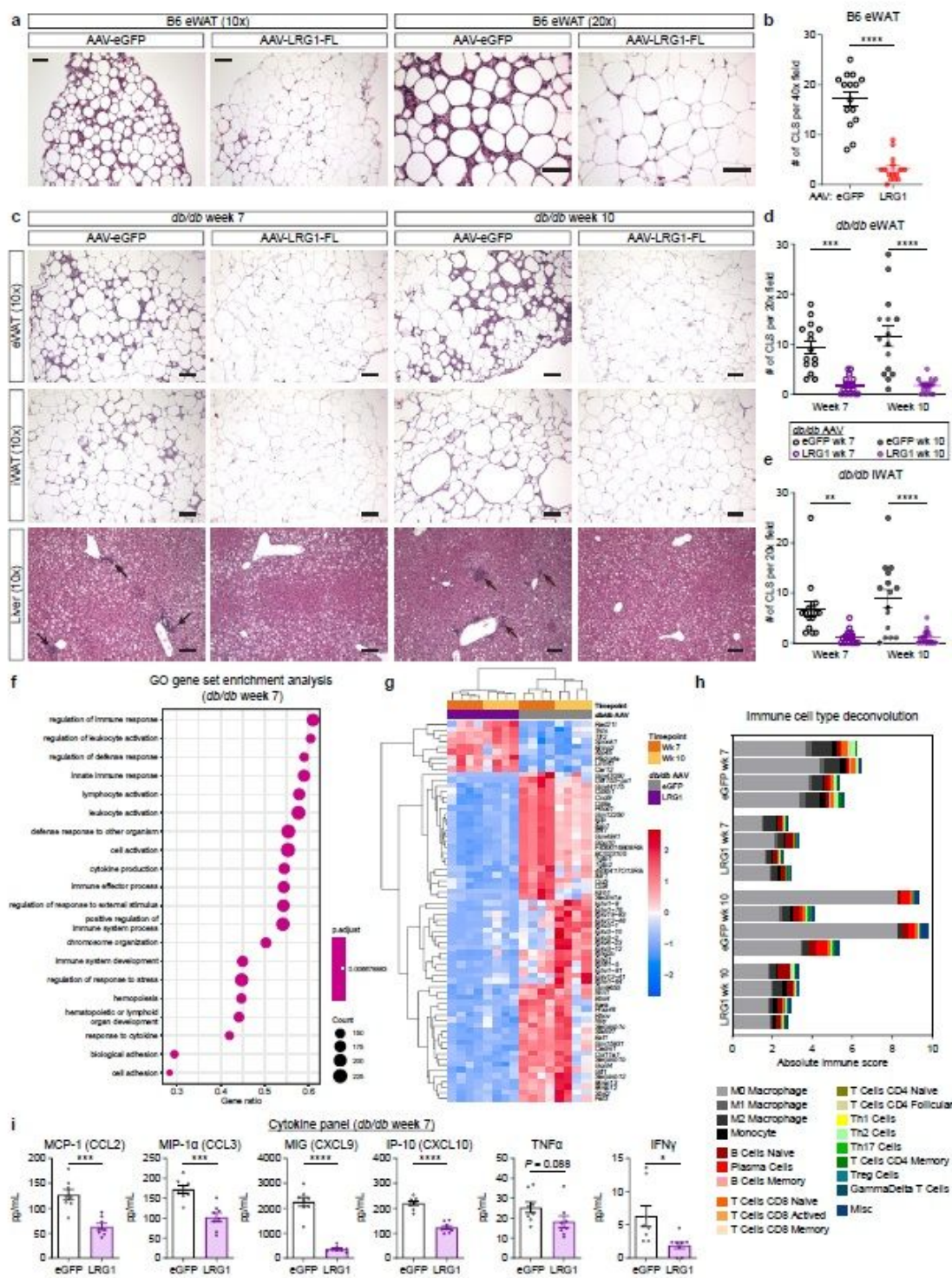


Figure 6

LRG1 suppresses obesity-associated systemic inflammation a, Representative images from H&E-stained eWAT sections from B6 DIO mice transduced with AAV-eGFP or AAV-LRG1-FL under 10x (left) and 20x (right) objectives. Scale bars indicate 100 μ m. b, Quantification of CLS from a. **** $P < 0.0001$ from two-sided Welch's t-test. 5 fields on a 40x objective from 3 animals were used for quantification ($n = 15$ per group). c, Representative images from H&E-stained eWAT, iWAT, and liver sections from db/db mice

transduced with AAV-eGFP or AAV-LRG1-FL. Arrows indicate liver inflammatory foci. Scale bars indicate 100 μ m. d,e, Quantification of CLS in eWAT (d) and iWAT (e) from c. Šídák post hoc test results from two-way ANOVA are indicated. **P < 0.01, ***P < 0.001, ****P < 0.0001. 5 fields under a 20x objective from 3 animals were used for quantification (n = 15 per group). f, Top 20 enriched GO BP pathways from GSEA of significantly differentially expressed genes between db/db-LRG1 and db/db-eGFP eWAT at 7 weeks of age. g, Heatmap of 68 differentially regulated genes (Log₂FC > 2 or < -2 and adjusted P < 0.01) between db/db-LRG1 and db/db-eGFP eWAT at both 7 and 10 weeks of age. h, Absolute scores from immune cell type deconvolution analysis of eWAT transcriptomes using CIBERSORTx. i, Quantification of serum chemokine/cytokine levels in db/db-LRG1 and db/db-eGFP at 7 weeks of age. *P < 0.05, ***P < 0.001, ****P < 0.0001 from two-sided Welch's t-test. n = 8 per group. Data are presented as mean \pm SEM.

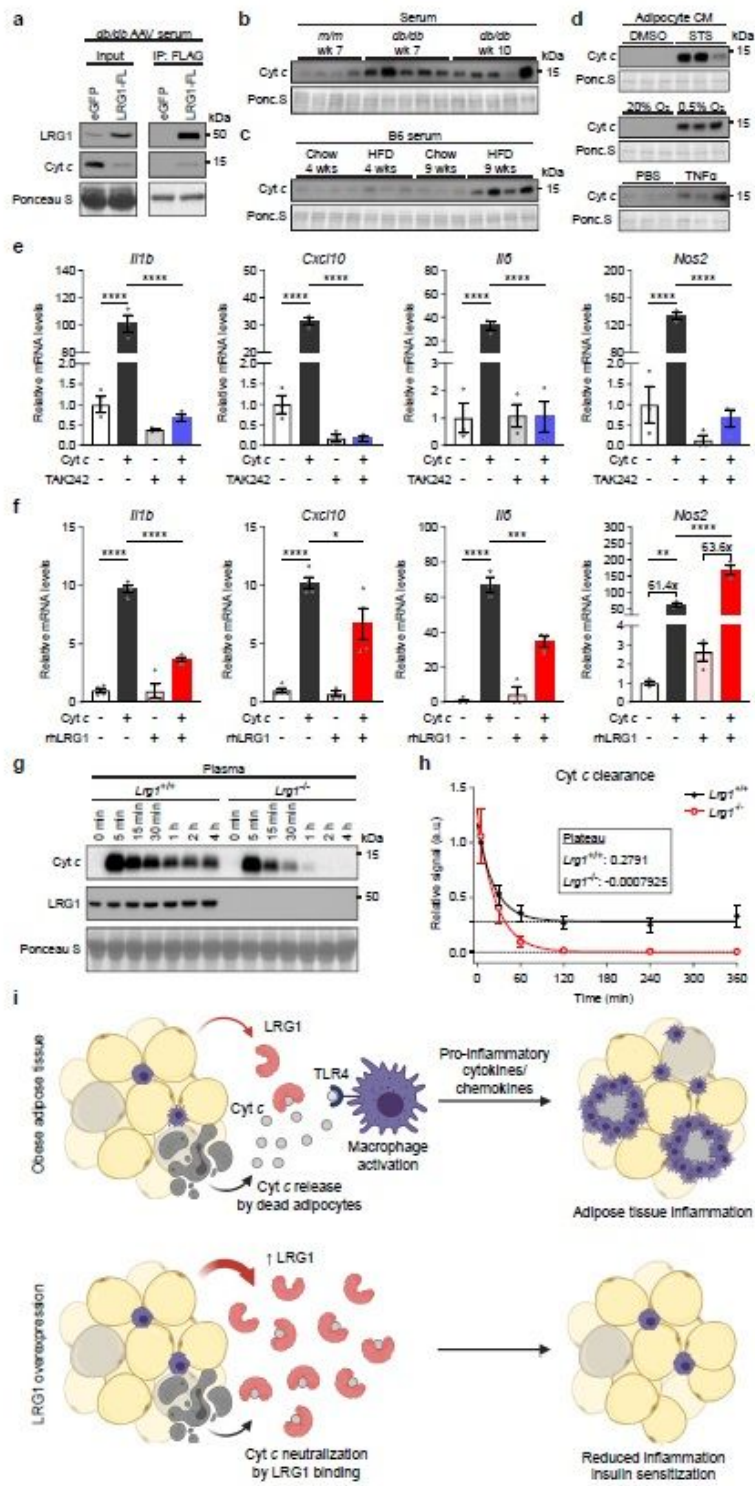


Figure 7

LRG1 binds extracellular cytochrome c and blocks its pro-inflammatory effect on macrophages a, α -FLAG co-IP of C-terminally FLAG-tagged LRG1 and Cyt c from the serum of AAV-transduced db/db mice at 7 weeks of age. b, Western blot of Cyt c in the serum of db/db or littermate m/m mice at 7 or 10 weeks of age. c, Western blot of Cyt c in the serum of B6 mice on standard chow or HFD for indicated weeks. HFD was started at 6 weeks of age. Developed from the same membrane in Fig. 3f. d, Western blot of Cyt c in

the CM of primary SubQ adipocytes under conditions promoting cell death. SubQ cells were treated with 1 μ M staurosporine (STS) or DMSO for 24 h (top); placed in normoxic or hypoxic chambers for 24 h (middle); or treated with 100 ng/mL recombinant TNF α or PBS without insulin for 24 h. Developed from the same membrane in Fig. 3i (bottom). e, Relative mRNA levels of a panel of pro-inflammatory genes in BMDMs in response to 30 μ g/mL equine Cyt c or 10 μ M TAK-242, a TLR4 inhibitor. BMDMs were treated with Cyt c or PBS for 6 h following 1 h pre-incubation with TAK-242 or DMSO. ****P < 0.0001 from Tukey post hoc test results following two-way ANOVA. n = 3 per group. f, Relative mRNA levels of a panel of pro-inflammatory genes in BMDMs in response to 20 μ g/mL equine Cyt c and 50 μ g/mL recombinant human LRG1. Indicated reagents or PBS were rotated for 1 h at RT prior to BMDM treatment for 6 h. *P < 0.05, **P < 0.01, ***P < 0.001, ****P < 0.0001 from Tukey post hoc test results following two-way ANOVA. n = 3-4 per group. g, Representative western blot of Cyt c in plasma of LRG1-KO and WT littermate male mice following retroorbital injection of 40 mg/kg equine Cyt c. h, Relative quantification of Cyt c intensities from g. Fitted one-phase decay curves and estimated values for the plateau are shown. n = 4 per group. i, Schematic depicting proposed mechanism. Data are presented as mean \pm SEM.

Supplementary Files

This is a list of supplementary files associated with this preprint. Click to download.

- [SupplementaryTable1.docx](#)
- [nreditrialpolicychecklistChoietalPC.pdf](#)
- [nrreportingsummaryChoietalv2PC.pdf](#)
- [LRG1ExtendedDataFiguresPrint.pdf](#)